The Journal of Physiology

The vascular geometry of the choriocapillaris is associated with spatially heterogeneous molecular exchange with the outer retina

Caitlin D. Faust[1], Christian A. Klettner[2], Marc Toso[1], Gregory S. Hageman[1], Ian Eames[2], Philip J. Luthert[3] and Moussa A. Zouache[1]

[1]*John A. Moran Eye Center, Department of Ophthalmology & Visual Sciences, University of Utah, Salt Lake City, Utah, USA*
[2]*Department of Mechanical Engineering, University College London, London, UK*
[3]*Institute of Ophthalmology, University College London, London, UK*

Handling Editors: Katalin Toth & Srikanth Ramaswamy

The peer review history is available in the Supporting information section of this article (https://doi.org/10.1113/JP285050#support-Information-section).

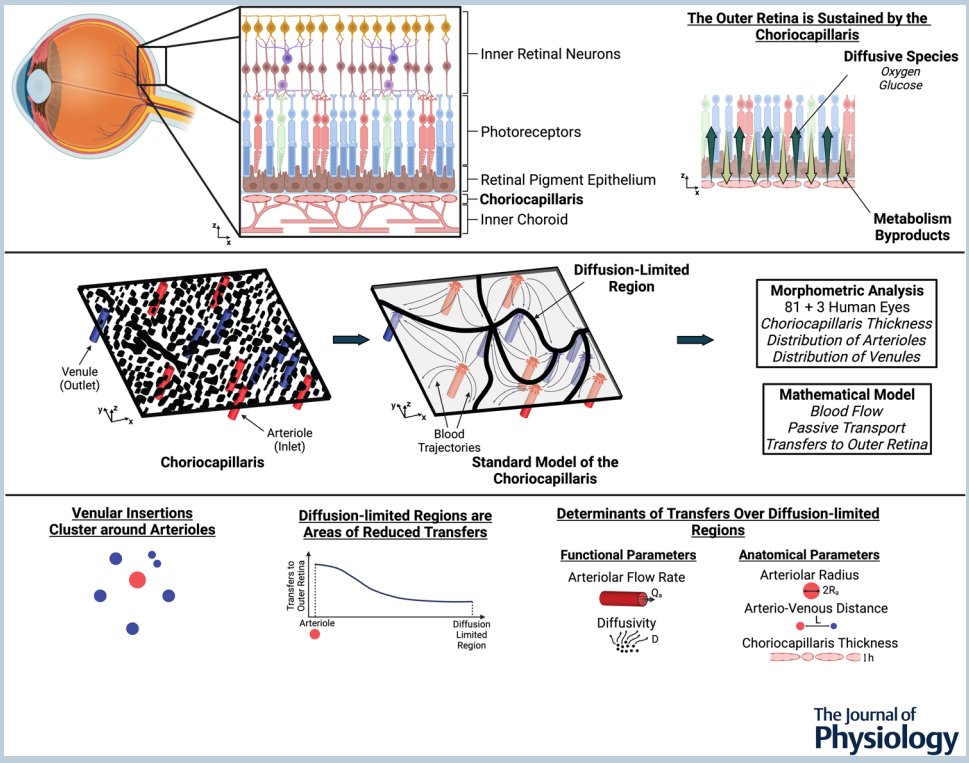

Abstract Vision relies on the continuous exchange of material between the photoreceptors, retinal pigment epithelium and choriocapillaris, a dense microvascular bed located underneath the outer retina. The anatomy and physiology of the choriocapillaris and their association with retinal homeostasis have proven difficult to characterize, mainly because of the unusual geometry of this vascular bed. By analysing tissue dissected from 81 human eyes, we show that the thickness of the choriocapillaris does not vary significantly over large portions of the macula or with age. Assessments of spatial variations in the anatomy of the choriocapillaris in three additional human eyes indicate

C. D. Faust and C. A. Klettner contributed equally as first authors.

DOI: 10.1113/JP285050

that the location of arteriolar and venular vessels connected to the plane of the choriocapillaris is non-random, and that venular insertions cluster around arteriolar ones. Mathematical models built upon these anatomical analyses reveal that the choriocapillaris contains regions where the transport of passive elements is dominated by diffusion, and that these diffusion-limited regions represent areas of reduced exchange with the outer retina. The width of diffusion-limited regions is determined by arterial flow rate and the relative arrangement of arteriolar and venular insertions. These analyses demonstrate that the apparent complexity of the choriocapillaris conceals a fine balance between several anatomical and functional parameters to effectively support homeostasis of the outer retina.

(Received 6 July 2023; accepted after revision 14 February 2024; first published online 20 March 2024)
Corresponding author M. A. Zouache: John A. Moran Eye Centre, Department of Ophthalmology & Visual Sciences, University of Utah, Salt Lake City, UT 84132, USA. Email: moussa.zouache@hsc.utah.edu

Abstract figure legend Adequate mass exchange between choriocapillaris and outer retina is necessary to sustain the photoreceptors and retinal pigment epithelium; two critical components of the visual system. The choriocapillaris has evolved a planar multipolar vascular geometry that differs markedly from the branched topology of most vasculatures in the human body. Using mathematical models and morphometric analyses of tissue collected from a large number of human eyes, we demonstrate that the geometry of the choriocapillaris is associated with spatially heterogenous molecular exchange with the outer retina. We also show that diffusion-limited regions, which represent areas of reduced exchange with the outer retina, are omnipresent over the plane of the choriocapillaris. Our data and analyses highlight a necessary balance between choriocapillaris anatomical and functional parameters to effectively support homeostasis of the outer retina and the visual process.

Key points

- The choriocapillaris is the capillary bed supporting the metabolism of photoreceptors and retinal pigment epithelium, two critical components of the visual system located in the outer part of the retina.
- The choriocapillaris has evolved a planar multipolar vascular geometry that differs markedly from the branched topology of most vasculatures in the human body.
- Here, we report that this planar multipolar vascular geometry is associated with spatially heterogenous molecular exchange between choriocapillaris and outer retina.
- Our data and analyses highlight a necessary balance between choriocapillaris anatomical and functional parameters to effectively support homeostasis of the outer retina.

Introduction

The main function of the choriocapillaris, the capillary bed of the choroidal vasculature (see Fig. 1*A*–*C*), is to support the metabolism of photoreceptor and retinal pigment epithelium cells, two major components of the visual system. It does so through the delivery of metabolism substrates to the photoreceptors

Caitlin Faust is pursuing an MD at the Spencer Fox Eccles School of Medicine, University of Utah. Caitlin completed her BS in biology with a minor in biomedical engineering at the University of Utah in 2020. Shortly after, she joined the clinical research team at the John A. Moran Eye Centre to study age-related macular degeneration under the mentorship of Gregory S. Hageman, PhD, and Moussa A. Zouache, PhD. She also worked as a clinical research coordinator at the Huntsman Cancer Institute, University of Utah, where she facilitated phase 1, 2 and 3 clinical trials in genitourinary cancers. **Christian Klettner** is a Lecturer in Thermofluids in the Department of Mechanical Engineering, University College London (UCL), London, UK. He received his PhD in Fluid Mechanics from UCL in 2010, which he followed with post-doctoral positions at the National University Health System, Singapore, and at UCL. Christian's research focuses on fundamental fluid flows and scalar transport, with a focus on Hele-Shaw configurations.

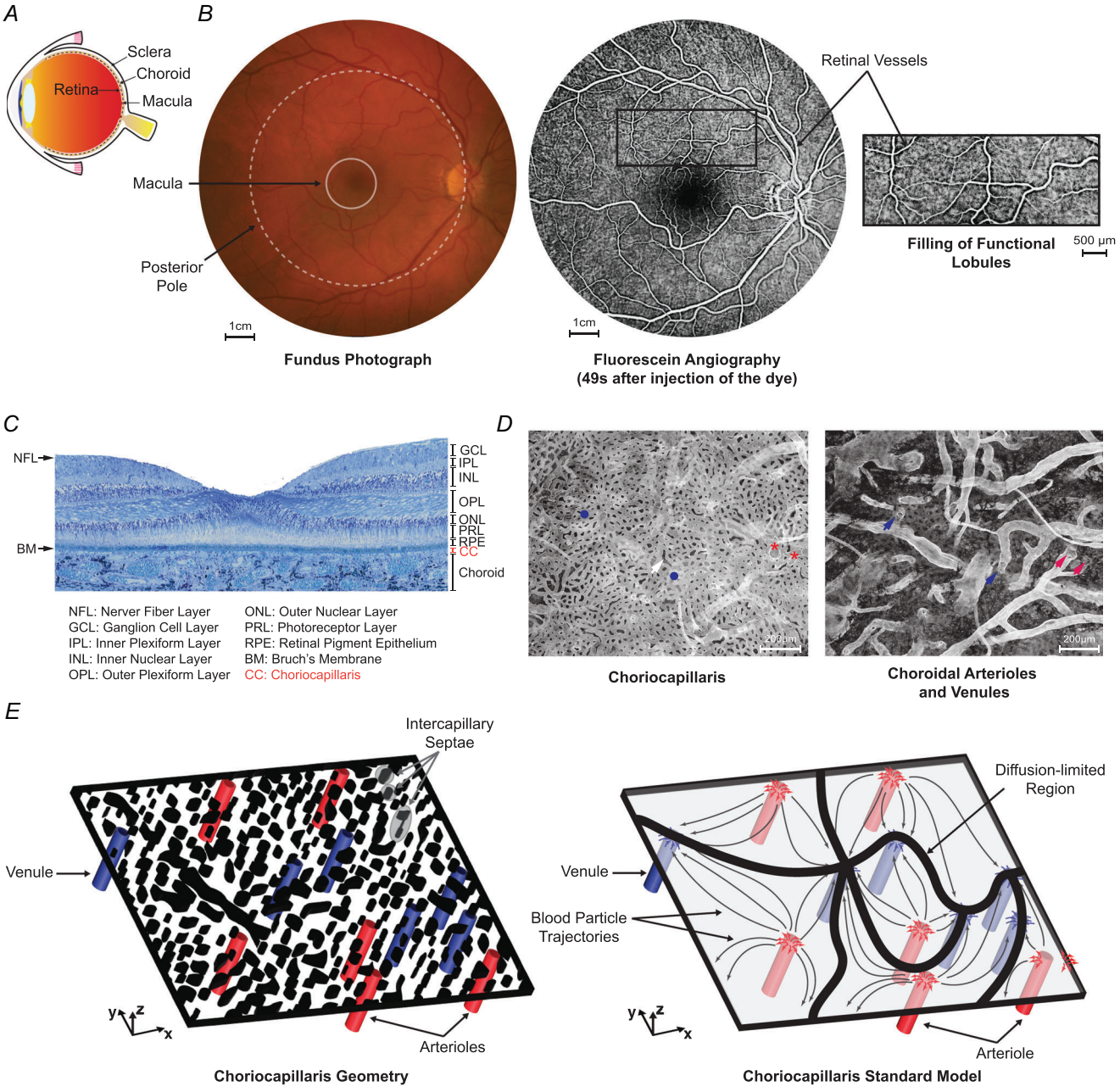

Figure 1. Location and vascular geometry of the choriocapillaris in humans
A, schematic of the human eye and its main elements in the posterior pole. *B*, fundus photograph and fluorescein angiogram captured in the right eye of the same healthy individual. The approximate location of the macula and posterior pole are highlighted. Local contrast enhancement was applied to the angiogram. The lobular filling of the choriocapillaris is visible in most of the posterior pole. Pigment in the macular region obscures the choriocapillaris, preventing the visualisation of the dye. *C*, histological section of the retina and choroid in the submacular area stained using Richardson's stain, with simplified description of retinal and choroidal layers. *D*, flat preparation of a portion of human choroid in the submacular area. The choriocapillaris is visualised in the left image; feeding vessels lying externally to the choriocapillaris are shown in the right image. The location of collagenous posts (septae) separating choriocapillaris vessels is highlighted with a white arrow. Insertions of arterioles (✻ and red arrows) and venules (● and blue arrow) are also shown. *E*, schematic illustrating the vascular geometry of the choriocapillaris and its simplified version. The choriocapillaris is modelled as two parallel sheets, with blood flowing between arterioles and venules inserted into its outermost plane. Septae are modelled as extrusions spanning the thickness of the channel. Their effect is not considered in the simplified geometry of the choriocapillaris (standard model).

(Linsenmeier & Braun, 1992; Niven & Laughlin, 2008; Wong–Riley, 2010), by clearing metabolic waste products from the subretinal space (Bill et al., 1983) and possibly by passively regulating the temperature of the back of the eye (Parver, 1991). Despite its key role in vision, our understanding of the choriocapillaris and its importance in maintaining photoreceptor homeostasis is limited. This is mainly due to its unusual anatomy, which has proven difficult to reconcile with *in vivo* visualisations of the blood flow within its plane and with frameworks describing mass exchange with the outer retina (Zouache, 2022). This lack of understanding has hindered our ability to determine the contribution of choriocapillaris impairments to the visual dysfunction associated with ageing and inflammatory and degenerative diseases of the back of the eye. Increasing age is associated with a general loss of choriocapillaris vessels and a possible reduction of its thickness (Zouache, 2022). In age-related macular degeneration (AMD), a primary cause of irreversible vision loss worldwide (Health Organisation, 2014; Wong et al., 2014), both structural (Mullins et al., 2011; Seddon et al., 2016; Spraul et al., 1996, 1999) and functional (Ciulla et al., 1999; Pauleikhoff et al., 1999; Mendrinos & Pournaras, 2009) changes have been reported. However, their significance is not well understood. The spatial selectivity displayed by pathologies associated with AMD has previously been linked to the specific anatomy of the choriocapillaris (Friedman et al., 1963; Müller, 1856; Tso, 1985; Wybar, 1954a) but it has thus far been difficult to confirm any associations.

The choriocapillaris has evolved a planar vascular geometry, which is uncommon among living organisms (LaBarbera, 1990). It fundamentally consists of a thin layer of densely organised capillaries contained between two continuous and approximately parallel sheets (see Fig. 1*C*–*D*). Blood enters and leaves the choriocapillaris through a set of arterioles and venules connected to the surface furthest from the retina approximately perpendicularly to the plane of the capillaries (see Fig. 1*D*). As a consequence of the vascular geometry of the choriocapillaris, the blood flow fundamentally consists of a planar multipolar flow (Zouache et al., 2016). One of the most striking features of this type of flows is that they are topologically decomposed into contiguous subsets separated by separation surfaces across which there is no flow (see Fig. 1*E*). Importantly, these separation surfaces are not physical but purely functional (Zouache et al., 2016); their location and shape can therefore not be readily identified in tissue. This segmentation of the choriocapillaris blood flow into functional vascular segments has been observed and described by ocular physiologists (Archer et al., 1970; Dollery et al., 1968; Flower, 1993; Flower et al., 1995; Hayreh, 1974a, 1974b, 1974c, 1975; Hirata et al., 2004; Hyvarinen et al., 1969; Kiryu et al., 1994; Perry et al., 1977) who commonly refer to groups of these units as lobules (Hayreh, 1974c). This term was initially introduced by analogy with the liver to characterize the relative arrangement of arterioles and venules being inserted into the plane of the choriocapillaris (Torczynski & Tso, 1976).

Vasculatures of the human body, such as those sustaining muscle and brain tissues, generally display branched geometries characterized by three-dimensionally distributed regions of transfer (LaBarbera, 1990) and local exchange approximately axisymmetric with respect to the axis of capillaries (Fletcher, 1978; Krogh, 1919a, 1919b; Murray, 1926; Ranvier, 1874; Spalteholtz, 1888; West et al., 1997). In contrast, the exchange of molecules between the choriocapillaris and the retina is planar and occurs across the plane that is closest to the retina (Zouache, 2022). These core differences limit our ability to use theoretical and experimental approaches traditionally applied to study blood flow and protein exchange in branched microvasculatures (Fletcher, 1978; Krogh, 1919a, 1919b; Murray, 1926; Ranvier, 1874; Spalteholtz, 1888; West et al., 1997) to the choriocapillaris. To address this, we have developed a theoretical framework to characterize the structure and function of this vascular bed, and how they may change in ageing and disease. This framework allowed us to show that the geometry of the choriocapillaris and blood flow patterns are associated with spatial heterogeneities in blood velocity and particle travel time across functional vascular segments (Zouache et al., 2015, 2016).

The impact of spatial heterogeneities in choriocapillaris blood flow on exchange with the retina and retinal homeostasis remains to be determined. Investigations of the structure and function of the choriocapillaris have thus far been limited and, in many ways, inadequate. Descriptions of the anatomy of the choriocapillaris (Ashton, 1952; Feeney & Hogan, 1961; Fryczkowski, 1994; Fryczkowski et al., 1991; Klien, 1966; Salzman, 1912; Torczynski & Tso, 1976; Wybar, 1954b; Yoneya et al., 1983; Zhang, 1994) have been mostly qualitative, with only a few studies (Fryczkowski, 1994; Olver, 1990; Ramrattan et al., 1994; Spraul et al., 1996, 2002; Torczynski & Tso, 1976) providing measurements of specific features in a limited number of human eyes. The absence of correlation between the anatomy of the choriocapillaris, its blood flow and mass transfers has made it difficult to identify the structural determinants of exchange with the outer retina. Various *in vivo* imaging methods have been applied to quantify choroidal blood flow in humans (Wei et al., 2018). However, these methods have not allowed for the characterization of blood flow patterns over meaningful length scales. Insights from experimental studies of choriocapillaris blood flow patterns carried out in animals (Flower et al., 1995; Kiryu et al., 1994; Perry et al., 1977;

Takasu et al., 2000; W. Flower, 1980) and are yet to be translated to humans.

The aim of this study was to examine the characteristics of protein exchange associated with the vascular geometry of the choriocapillaris. A standard model of this capillary bed is used to predict the salient features of exchange with the outer retina and to identify their key anatomical and functional determinants. Two of these determinants, the relative arrangement of arteriolar and venular insertions into the plane of the choriocapillaris and its thickness, are characterized using a total of 84 human donor eyes. These measurements and the standard model of the choriocapillaris are then combined to characterize exchange of passively transported molecules, their spatial heterogeneity and the functional and structural constraints necessary for the adequate support of the metabolic requirements of the outer retina.

Methods

Standard model of the choriocapillaris

The methodology applied in this study is described in Fig. 2. The vascular geometry of the choriocapillaris and the mathematical framework used to describe the blood flow and the transport of passive elements within its plane have been described previously (Zouache et al., 2016). The choriocapillaris fundamentally consists of a thin planar sheet of capillaries (see Fig. 1*C*,*D*), which occupy between 50 and 75% of its volume (Ramrattan et al., 1994). Non-vascular volume is occupied by inter-capillary septae of various shapes and sizes (Fig. 1*D*). The choriocapillaris is therefore modelled as two parallel planar sheets separated by a width h, which is assumed to be constant over the length of a functional vascular segment (Fig. 3*B*). The space between capillaries is represented by extrusions perpendicular to the plane of the choriocapillaris spanning the thickness of the channel (Fig. 1*E*). Blood enters and leaves the choriocapillaris through a set of arterioles and venules connected to the surface furthest from the retina approximately perpendicularly to the plane of the capillaries. Arteriolar and venular insertions are therefore modelled as cylindrical vessels of radius R_a and R_v, respectively, connected to the same sheet perpendicularly to the plane of the choriocapillaris. The anatomical arrangement of these insertions is a key determinant of the shape of

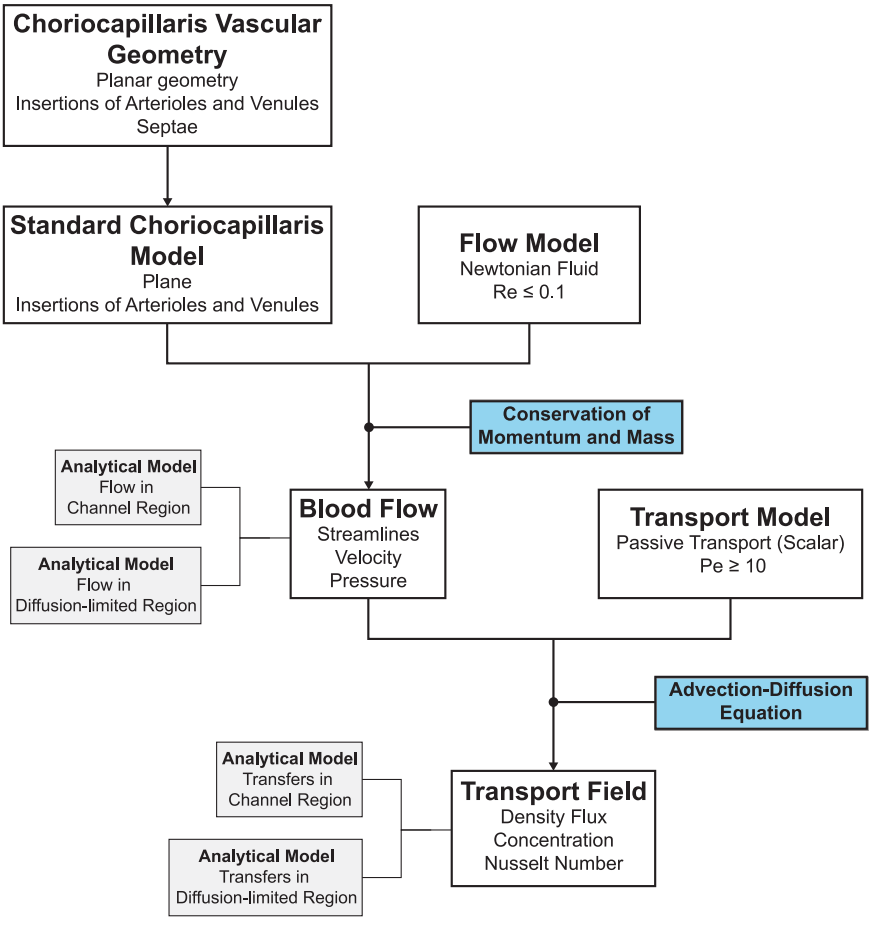

Figure 2. Flow chart describing the methodology employed to model the geometry of the choriocapillaris and determine blood flow, transport field and exchange with outer retina
The conservation of momentum and mass and the convection–diffusion equation were solved over a standard model of the choriocapillaris consisting of two parallel sheets separated by a distance denoted h and connected to a series of inlet and outlet pipes (illustrated in Fig. 1*E*). Blood was modelled as a Newtonian fluid with uniform kinematic viscosity (denoted ν). The characteristic Reynolds number over the choriocapillaris $Re \sim \frac{\bar{u}h}{\nu}$, where $\bar{u}$ is the mean blood velocity, decreases rapidly with distance from arteriolar insertions. A simplified model that does not account for reactions that may occur in blood was used to describe mass transport. Particles were modelled as a passive scalar characterised by a diffusivity denoted D. The characteristic Péclet number over the choriocapillaris $Pe \sim \frac{\bar{u}h}{D}$ decreases rapidly with distance from arteriolar insertions.

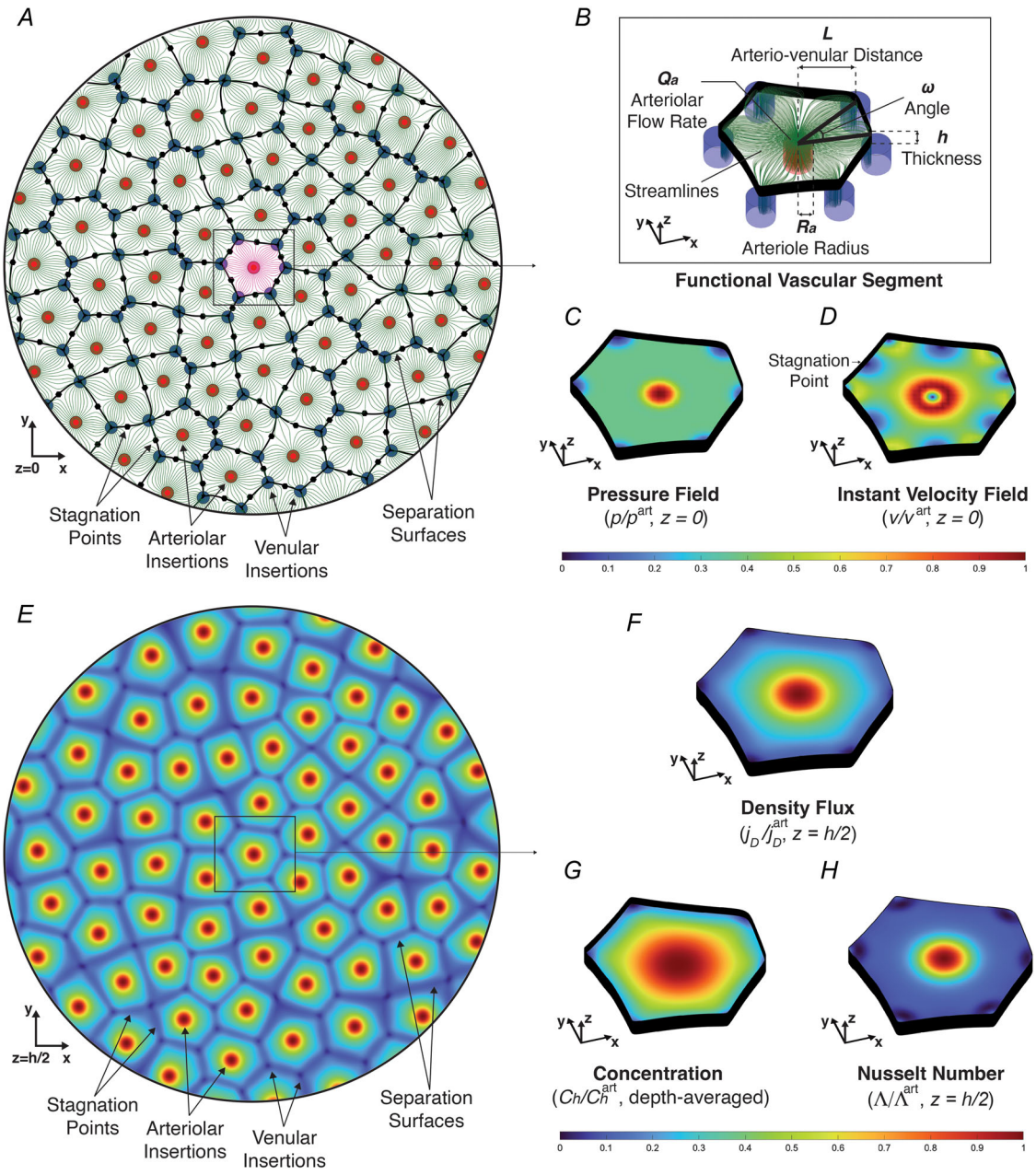

Figure 3. Salient features of the blood flow, passive transport and transfers across the choriocapillaris
Equations for the flow and transport of passive elements were solved over three-dimensional domains consisting of a thin channel of thickness h connected to inlet and outlet pipes through its lower surface (Fig. 1*E*). *A*, streamlines of the flow field (green) extracted in the mid-plane of the channel ($z = 0$) for a random distribution of arteriolar (red) and venular (blue) insertions. Surfaces separating subsets of the flow field are plotted as black lines. *B*, three-dimensional streamlines within the functional vascular segment highlighted in (*A*) showing the geometrical and functional parameters included in the mathematical framework. The angle ω describes the relative arrangement of arteriolar and venular insertions. *C, D*, contour maps of the mid-plane ($z = 0$) pressure and instant velocity fields for the subset highlighted in (*A*). These two diagnostics were normalized by their value at the arteriolar insertion. *E*, contour of the density flux j_D generated for a Péclet number $P\,e_a = 100$ associated with the randomly generated distribution of arteriolar and venular insertions shown in (*A*). *F*, density flux across the upper sheet ($z = h/2$) shown for the subset highlighted in (*E*). *G, H*, contour maps of the depth-averaged concentration and Nusselt number in the mid-plane and upper surface of the randomly generated geometry, respectively. In (*E–H*) all measures were normalized by their value at the arteriolar insertion of each functional vascular segment.

functional vascular segments (Zouache et al., 2016); it is here described by the distance between the arteriolar insertion supplying a functional segment and a venular opening draining it, which is denoted L, and by the angle between this arteriolar insertion and two consecutive venular openings draining it, which is here denoted ω (see Fig. 3*B*). Within this model, the flow is entirely determined by pressure gradients and viscous forces, which fits experimental observations (Flower et al., 1995). Septae do not fundamentally modify the blood flow properties associated with multipolar flows, as their effect is mainly local (Zouache et al., 2016). Since the goal of this study is to characterize the features of mass transfers associated specifically with the vascular geometry of the choriocapillaris, intercapillary septae are not modelled.

Model for the flow through the choriocapillaris

Blood is a non-Newtonian fluid whose viscosity is determined by plasma viscosity, erythrocyte deformability and aggregation and haematocrit. At smaller scales (blood vessels less than 300 μm in diameter), blood displays Newtonian characteristics and has a bulk haematocrit-dependent viscosity (Replogle et al., 1967; Pries et al., 1994). Here, blood is modelled as a Newtonian fluid with uniform kinematic viscosity ν. The Reynolds number associated with the inlet arteriole flow is

$$Re_a = \frac{Q_a}{\nu R_a} \tag{1}$$

where Q_a is the flow rate at the arteriole. The characteristic Reynolds number over the choriocapillaris $Re \sim \frac{\bar{u}h}{\nu}$, where $\bar{u}$ is the mean blood velocity, decreases rapidly from the arteriolar insertion. It typically satisfies $Re \lesssim 0.1$ (Zouache et al., 2015, 2016) so that the flow is viscously dominated and inertial effects are negligible (Lighthill, 1972). The blood flow is steady and solely determined by the balance between pressure gradients and viscous forces, something that was experimentally observed by Flower et al. (1995). The flow is described by the conservation of mass and momentum

$$\nabla \cdot \mathbf{u} = 0, \tag{2}$$

$$\rho\,(u \cdot \nabla)\,u = -\nabla p + \nabla \cdot \tau, \tag{3}$$

where u is the blood velocity field and τ is the Newtonian viscous stress tensor. The flow at the arteriolar openings is assumed to be fully developed and is imposed to be

$$u = \frac{2Q_a}{\pi R_a^2}\left(1 - \left(\frac{r}{R_a}\right)^2\right)\hat{z}, \tag{4}$$

where r is the radial coordinate measured from the centre of the vessel and $\hat{z}$ is a unit vector perpendicular to the surface of the inlet. For simplicity and without loss of generality, the pressure at venular openings is imposed to be zero in all numerical resolutions. The no-slip boundary condition $u = 0$ is imposed on the upper and lower surfaces of the channel and on the surface of the inlet and outlet pipes.

Modelling framework for the transfer of molecules

The transport of molecules in the choriocapillaris occurs through a combination of advection, diffusion and reaction. The ratio of advective to diffusive transport is described by the Péclet number. The Péclet number associated with the inlet arteriole flow is

$$Pe_a = \frac{Q_a}{DR_a} = \frac{\nu Re_a}{D}, \tag{5}$$

where D is the molecular diffusivity. The characteristic Péclet number over the choriocapillaris $Pe \sim \frac{\bar{u}h}{D}$ varies spatially with the mean local velocity. Transport in blood is dominantly diffusive if $Pe \ll 1$; it is dominated by advection when $Pe \gg 10$. Since our goal is to characterize the salient features of transfers across the choriocapillaris, we use a simplified model of mass transport that does not account for reactions that may occur in blood. Particles are modelled as a passive scalar, and transport is described by the convection-diffusion equation

$$\nabla \cdot (uC) = \nabla \cdot (D\nabla C), \tag{6}$$

where C is the concentration of the compound considered. The concentration/scalar is set to $C = C_0$ at the arteriole. Only diffusive transfers from blood are considered in this study. These transfers occur across the surface of the choriocapillaris that is closest to the retina; therefore, we impose the no-flux boundary condition

$$n \cdot D\nabla C = 0, \tag{7}$$

where n is a unit vector perpendicular to the surface of the choriocapillaris connected to arterioles and venules. We also impose this no-flux condition on the outer surface of arterioles and venules. A Dirichlet boundary condition of the form

$$C\left(x, y, \frac{h}{2}\right) = C_1 \tag{8}$$

is imposed on the surface of the choriocapillaris closest to the outer retina. We define the mass density flux and the normalized mass density flux (called the Schmidt or Nusselt number) as

$$j_D = -D\nabla C \cdot \hat{z}, \quad \Lambda = \frac{j_D h}{DC_h}, \tag{9}$$

respectively, where the depth-averaged concentration C_h is defined as

$$C_h = \frac{1}{h} \int_{-\frac{h}{2}}^{\frac{h}{2}} C \mathrm{d}z. \tag{10}$$

The Nusselt number may be determined from the profile of the concentration across choriocapillaris cross-sections. Away from the entrance region, mass transfer is fully developed, and the Nusselt number converges to a constant value here denoted Λ_∞. Departure from this value is described by the parameter $\bar{\Lambda}$, defined as

$$\bar{\Lambda} = \frac{\Lambda - \Lambda_\infty}{\Lambda_\infty}. \tag{11}$$

Solutions for the flow and passive transport

Equations for the flow (eqn (2) and eqn (3)) and for the transport of passive elements (eqn (6)) were solved numerically over the three-dimensional standard model of the choriocapillaris consisting of two parallel sheets connected to inlet and outlet pipes (shown in Fig. 1*E*). Typically, more than 25 points across the thickness of the space between sheets and across the pipe radii were used to resolve the flow and scalar fields in three-dimensional numerical simulations. The flow domain was meshed using the software Gmsh (Geuzaine & Remacle, 2009). Between 300,000 and 2,000,000 nodes were used in the computations. The system of equations (eqn (2) and eqn (3)) and eqn (6) were numerically solved using OpenFoam (*simpleFoam* solver for hydrodynamics and *scalarTransportFoam* solver for scalar transport). All numerical schemes were second-order accurate. The defining equations were solved in two steps: involving first the calculation of the velocity field until the flow field ran to steady state; the second step was to determine the scalar field for the boundary conditions (eqn (7) and eqn (8)).

Analytical model for flow and transfers in channel regions

Away from an arteriolar insertion, the flow is a channel flow approximately axisymmetric with respect to the axis of the arteriolar insertion. In this *channel region*, the magnitude of the radial velocity satisfies

$$u_r = \frac{Q_a}{2\pi h r}, \tag{12}$$

where r is the radial distance from the centre of the arteriolar insertion. A solution to eqn (6) in this region is (Zouache et al., 2019)

$$C_h = C_h^0 \exp\left(-\frac{2D\Lambda_\infty}{\beta Q_a h} r^2\right), \quad j_D = \frac{D\Lambda_\infty}{h} C_h^0 \exp\left(-\frac{2D\Lambda_\infty}{\beta Q_a h} r^2\right), \tag{13}$$

where r is the radial distance from the centerline of the arteriolar insertion, C_h^0 is the concentration at $r = 0$, $\beta \simeq 1.03$ and $\Lambda_\infty \simeq 2.5694$.

Analytical model for flow and transfers in diffusion-limited regions

Diffusion-limited regions connect two venular insertions to a stagnation point (Zouache et al., 2016). Without loss of generality, we consider a separation surface parallel to the horizontal axis x centred at its stagnation point, as shown in Fig. 6*A*. The flow is dominantly an irrotational straining flow where the velocity, to the leading order, satisfies

$$u_x = \frac{3}{2}\kappa x\left[1 - \left(\frac{z}{h/2}\right)^2\right], \; u_y = \frac{3}{2}\kappa y\left[1 - \left(\frac{z}{h/2}\right)^2\right], \; u_z = 0, \tag{14}$$

where κ is a strain rate. This strain rate may be approximated by considering variation in the velocity in the direction perpendicular to the separation surface (Zouache et al., 2019), which yields

$$\kappa = \left.\frac{\partial u_x}{\partial x}\right|_{x\to 0} \simeq \frac{Q_a}{\pi h L^2 \sin^2\left(\frac{\omega}{2}\right)}. \tag{15}$$

A solution to eqn (6) in the vicinity of a separation surface for sufficiently large Péclet numbers is (Zouache et al., 2019)

$$C_h = \frac{C_h^s}{{}_1\mathcal{H}_1\left[\frac{1}{2}\left(-1 - \frac{\Lambda_\infty}{2h^2}w^2\right); \frac{1}{2}; 1\right]} \exp\left(-\frac{y^2 - w^2}{w^2}\right) {}_1\mathcal{H}_1\left[\frac{1}{2}\left(-1 - \frac{\Lambda_\infty}{2h^2}w^2\right); \frac{1}{2}; \frac{(w-y)^2}{w^2}\right], \tag{16}$$

$$j_D = \frac{\Lambda_\infty D C_h^s}{{}_1\mathcal{H}_1\left[\frac{1}{2}\left(-1 - \frac{\Lambda_\infty}{2h^2}w^2\right); \frac{1}{2}; 1\right] h} \exp\left(-\frac{y^2 - w^2}{w^2}\right) {}_1\mathcal{H}_1\left[\frac{1}{2}\left(-1 - \frac{\Lambda_\infty}{2h^2}w^2\right); \frac{1}{2}; \frac{(w-y)^2}{w^2}\right]. \tag{17}$$

where ${}_1\mathcal{H}_1$ is the Kummer confluent hypergeometric function (Abramowitz & Stegun, 1972),

$$w = \sqrt{\frac{2D}{\beta\kappa}} \tag{18}$$

is the width of the diffusion-limited region, and C_h^s is the concentration at the boundary between the channel region and diffusion-limited region; $C_h^s = C_h\,(y = w)$. Within the range of Péclet numbers and distances between

arteriolar and venular openings considered, $y \ll 1$. A Taylor series expansion of eqn (16) and eqn (17) yields

$$j_D = \frac{\Lambda_\infty D C_h^s}{{}_1\mathcal{H}_1\left[\frac{1}{2}\left(-1-\frac{\Lambda_\infty}{2h^2}w^2\right);\frac{1}{2};1\right]h}\left(1+\frac{\Lambda_\infty}{2h^2}(w-y)^2\right). \quad (19)$$

Combining eqn (18) and eqn (15) yields

$$w^2 \sim \frac{2\pi DhL^2\sin^2\omega/2}{Q_a}. \quad (20)$$

Comparison between channel and diffusion-limited regions

To compare transfers in diffusion-limited regions to those in channel regions, we consider the variation of the density flux j_D along the streamline connecting an arteriolar insertion to a stagnation point (see Fig. 6*A*). The entrance of the channel region is $r_0 = 0$ while the entrance of the diffusion-limited region, which is also the border between the channel and diffusion-limited regions, is $r_1 = L\cos(\frac{\omega}{2}) - w$. The outer boundary of the diffusion-limited region intersects with the stagnation point at $r_2 = L\cos(\frac{\omega}{2})$. We compare the density flux in the two regions by defining

$$\bar{j}_D^{DL} = \frac{j_D - j_D(r=r_2)}{j_D(r=r_1) - j_D(r=r_2)},\ \bar{r}^{DL} = \frac{r-r_1}{r_1-r_2}, \quad (21)$$

$$\bar{j}_D^{C} = \frac{j_D - j_D(r=r_1)}{j_D(r=0) - j_D(r=r_1)},\ \bar{r}^{CR} = \frac{r}{r_0-r_1}. \quad (22)$$

These parameters describe a density flux independent of differences in the concentration at the entrance and exit of the channel and diffusion-limited regions and normalized by the width of these two regions, respectively. As w tends to L, the concentration at the entrance of the diffusion-limited region becomes small so that transfers do not occur across this area. Therefore, only the case $w \ll L$ is considered.

Human donor eyes

Eighty-one of the human donor eyes used in this study were collected at the Department of Ophthalmology & Visual Sciences, University of Iowa, Iowa City, Iowa, USA, between 2002 and 2007 and at the John A. Moran Eye Centre, University of Utah, Salt Lake City, USA, between 2007 and 2020 in collaboration with local hospitals and eye banks, and were held at the Sharon Eccles Steele Centre for Translational Medicine, John A. Moran Eye Centre. Three additional eyes were obtained from the Moorfields Eye Bank, Institute of Ophthalmology, University College London, London, UK; these had been collected between 2012 and 2018. All participants were willing eye donors, and written informed consent was obtained from surviving relatives. The study adhered to the *Declaration of Helsinki* and was approved by the Institutional Review Boards of the University of Iowa, University of Utah and University College London. Demographic information including sex, date of birth and ethnicity was recovered from patient health records. All subjects selected for this study were of European ancestry and unrelated. The presence of ocular pathology was assessed in all eyes using gross photographs of whole globes by the same experienced investigator.

Histology of human donor eyes

All 81 eyes obtained from the Sharon Eccles Steele Centre for Translational Medicine, John A. Moran Eye Centre, University of Utah, were collected within 5 h of death and processed following the same protocol. Upon receipt of donor eyes, circular portions of anterior segments (which included the retina and choroid) were dissected at the same location and fixed in 50% dilute strength Karnovsky's fixative until further processing. For each donor, tissue samples from one randomly selected eye were removed from storage and 4 mm biopsy punches were dissected in the macular region. The punches were washed three times in 0.1 M cacodylate buffer and post-fixed in 2% osmium tetroxide (Cat #19192, Electron Microscopy Science, USA). They were then dehydrated in an ethanol series and brought to 100% propylene oxide (Cat #20412, Electron Microscopy Science, USA). The tissue was embedded in Epon and cured overnight at 60°C. Sections 1 μm thick were subsequently cut and stained with Richardson's stain, before being viewed and photographed under a light microscope.

Segmentation and quantification of histology sections

The lumen of every capillary in the plane of the choriocapillaris, presenting normal endothelial cells, was manually delineated by the same observer using an in-house ImageJ (Abramoff et al., 2004) macro; see Fig. 5*F*. The coordinates of each point was saved, exported as overlays and stored in text files. Quantification of choriocapillaris features was performed using the software Matlab R2020a (MathWorks, Massachusetts, United States). The inner and outer surfaces of the choriocapillaris were delineated by determining the boundary enclosing all choriocapillaris vessels. A shrink factor of 0.4 was used to ensure that this boundary was tangent to choriocapillaris vessels. One section only was selected for quantification for each eye. The variation of the thickness of the choriocapillaris with distance from the fovea was determined by calculating the minimum Euclidian distance between the inner and outer borders

of the choriocapillaris across each section. This thickness was sampled at approximately 5000 points for each section. Mean choriocapillaris thickness was calculated by averaging thicknesses measured at each of these points across sections. The 95% confidence interval was determined by calculating the standard error of the mean at each point, multiplying it by the calculated 95% values of the *t*-distribution and adding and subtracting these values from the mean. Associations between age and mean choriocapillaris thickness were assessed using linear regressions.

Whole-choroid immunohistochemistry

Eyes obtained from the Moorfields Eye Bank were fixed in 4% paraformaldehyde (PFA) 24–50 h after death and stored in saline in a fridge at 4°C. Tissues including the retina and choroid were dissected from the macular region of each eye. After gently detaching retinas, the remaining retinal pigment epithelium/choroids were washed in 0.1 M PBS and incubated in 0.5% trypsin + EDTA (Life Technologies Ltd, UK) at room temperature for 15 min, before gently brushing the retinal pigment epithelium under a dissection microscope. The remaining choroids were washed three times in 0.1 M PBS and incubated for 2 h with FITC-labelled UEA-I (Vector Laboratories, USA). The samples were thereafter washed five times in 0.1 M PBS and then in TBS, mounted using an anti-fade mounting medium (Vector Laboratories, USA) and imaged using the Zeiss 710 LSM (Zeiss, Germany) confocal microscope. The imaging of large portions of tissue required the sequential imaging of adjacent tiles and their subsequent stitching in post-processing, which was carried out using the Zen software package (Zeiss, Germany).

Identification of arteriolar and venular insertions and pattern analysis

Maps of arteriolar and venular insertions were generated as previously described (Zouache et al., 2016). Briefly, insertions of intermediate choroidal vessels into the choriocapillaris, which appear as round or oval openings in its outermost plane, were first identified. These insertions were classified as arteriolar or venular based upon the nature of the intermediate choroidal vessel servicing it. Arterioles and venules were distinguished according to endothelial cell morphology or based on their branching pattern and/or trajectory in the deep and superficial choroid. The location of arteriolar and venular insertions was registered using Matlab R2020a (MathWorks, Massachusetts, United States). The software was also used to identify the nearest arteriolar and venular insertions for each arteriolar insertion. Point pattern analyses were performed using R (Team, 2021) and the package *spatstat* (Baddeley & Turner, 2005). The pair correlation function (Baddeley et al., 2015), denoted *g*, was used to identify patterns of repulsion or attraction between arteriolar and venular insertions. The range of angles between an arteriolar insertion and two consecutive venular ones (denoted ω; see Fig. 3*B*) was determined by estimating the ratio between these two types of insertion and using the relation (Zouache et al., 2016)

$$\omega = \frac{N_a}{N_a + N_v}\,\pi, \tag{23}$$

where N_a is the number of arteriolar insertions and N_v is the number of venular insertions. Importantly, this relation assumes that functional vascular segments form regular polygons; it therefore only provides an approximate value for ω. Because of local variations in the distribution of arteriolar and venular insertions, ω was estimated for each arteriolar insertion. To do so, we counted the number of venular insertions N_v located within a radius $r = 2r^{\frac{a}{v}}_{med}$ from each arteriolar insertion, where $r^{\frac{a}{v}}_{med}$ consisted of the median distance between arteriolar and venular insertions within the sample.

Literature review for functional parameters

The primary aim of the literature review was to collect functional measurements made in the choriocapillaris of healthy individuals and primates. Searches were undertaken in the PubMed and Scopus databases from their inception to 15 July 2022. The terms 'choriocapillaris,' 'choroid' and 'lobule' were searched for individually and combined with the terms 'physiology,' 'angiography,' 'functional,' 'anatomical,' 'fluorescein,' 'indocyanine green,' 'blood flow,' 'corrosion cast' and 'immunohistochemistry.' A list of relevant ophthalmology books was established and searched manually. Reference lists were hand-searched and citations of articles of interest were screened. Approximate measurements, ranges, means, standard deviations and regions of the eye where measurements were performed were extracted. Images of fluorescein or indocyanine green (ICG) angiograms of the choriocapillaris were systematically extracted and processed to collect information on functional features of the choriocapillaris. Studies designed to test the effect of pharmacological compounds on choriocapillaris blood flow were excluded. Data generated using optical coherence tomography angiography devices were excluded because of the current lack of correlation between the measurements that these devices provide and choriocapillaris' anatomical and functional features.

Results

Salient features of mass transfers across functional vascular segments

Functional vascular segments may be fundamentally decomposed into three separate regions with distinct salient flow and mass transfer properties (see Fig. 4 and Table 1). Close to arteriolar insertions the flow transitions from a pipe flow to a channel flow. Within this *turning* region, the transport of passive elements is dominated by vertical diffusion. An approximate similarity solution may be obtained for the advection–diffusion equation (Zouache et al., 2019), which yields

$$j_D \sim \left(D^2\gamma\right)^{1/3}, \tag{24}$$

where γ is a strain rate and D is the diffusivity of the molecule considered. Refined numerical simulations (Zouache et al., 2019) showed that γ is a function the ratio between the radius of the efferent arteriole and the thickness of the choriocapillaris $\delta = \frac{R_a}{h}$, with $\gamma \sim \delta$ for $\delta \leq 1$ and $\gamma \sim \exp(\delta)$ for $\delta > 1$. It is therefore partly determined by the geometry of the arteriolar insertion into the choriocapillaris.

Away from the turning region, the flow is a channel flow approximately axisymmetric with respect to the axis of the arteriolar insertion. In this *channel region*, the magnitude of the radial velocity decreases inversely with distance from the centre of the arteriolar insertion. In the region, where mass transfer is fully developed, the Nusselt number converges to the constant value $\Lambda_\infty \simeq 2.5694$. The density

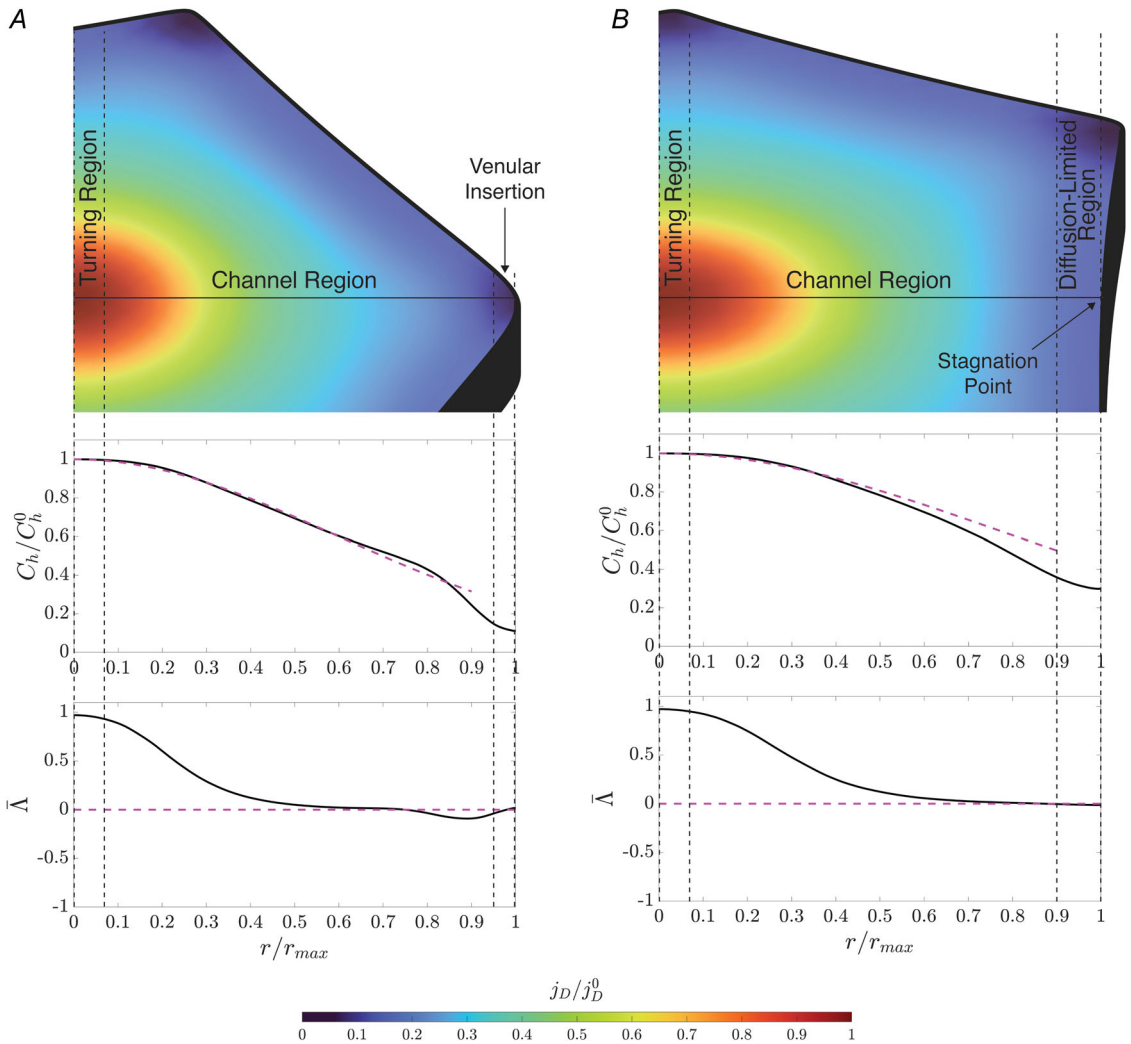

Figure 4. Salient features of diffusive transfers across a choriocapillaris functional vascular segment
The variation of the depth-averaged concentration C_h normalized by $C_h^0 = C_h(r = 0)$ and $\bar{\Lambda} = \frac{\Lambda - \Lambda_\infty}{\Lambda_\infty}$ along a line joining an inlet and (*A*) a venular insertion or (*B*) a stagnation point is plotted. The distance from the inlet r was normalized by the length of each line, denoted r_{max}. The distribution of the mass density flux j_D normalized by $j_D^0 = j_D(r = 0)$ is also shown for both configurations. Dashed lines represent variations obtained with analytical models (eqn (13)).

Table 1. Structural and functional determinants of mass transfers in the choriocapillaris and models describing their salient features

Region	Anatomical determinants	Functional determinants	Model
Turning region	$R_a,\ h$	$Q_a,\ D$	$j_D \sim (D^2\gamma)^{1/3}$
	$\delta = R_a/h$		$\gamma \sim \delta\ (\delta \leq 1);\ \gamma \sim \exp(\delta)\ (\delta > 1)$
Channel region	$R_a,\ h,\ L$	$Q_a,\ D$	$j_D \sim \frac{D\Lambda_\infty}{h} \exp(-\frac{r^2}{R_a h Pe_a})$
Diffusion-limited region	$R_a,\ h,\ L$	$Q_a,\ D$	$j_D \sim 1 + \frac{\Lambda_\infty}{2h^2}(w-y)^2$
			$w \sim 2\pi DhL^2\sin^2(\omega/2)/Q_a$

R_a radius of efferent arteriole; h, choriocapillaris thickness; L distance between arteriolar and venular insertion; ω angle between the arteriolar insertion and two consecutive venular insertions; Q_a arteriolar flow rate; D molecular diffusivity.

flux is mainly determined by the concentration field, the diffusivity of the compound considered and the thickness of the choriocapillaris, i.e.

$$j_D \sim \frac{D\Lambda_\infty}{h} C_h, \tag{25}$$

where C_h is the concentration averaged over a channel cross-section.

The boundaries between functional vascular segments, which connect two venular openings to a stagnation point (Zouache et al., 2016), display transport properties that differ markedly from the turning and channel regions. The velocity in the direction perpendicular to these separation surfaces tends to zero with distance to these surfaces. As a result, the passive transport in their vicinity is dominated by diffusion. Another consequence is that the travel time of fluid particles close to these surfaces increases with distance from it, and is theoretically infinite on it. Within diffusion-limited regions the mass density flux scales as (Zouache et al., 2019)

$$j_D \sim 1 + \frac{\Lambda_\infty}{2h^2}\left(w-y\right)^2, \tag{26}$$

where $y = w$ corresponds to the boundary between the channel region and the diffusion-limited region and $y = 0$ is the coordinate of the stagnation point on the surface separating two functional vascular segments (see Figs 4 and 6).

The relative size of the turning, channel and diffusion-limited regions and their differential contribution to exchange with the outer retina are determined by both functional and anatomical parameters (summarized in Table 1). Estimates of these parameters are sought in the next sections.

Relative arrangement of arteriolar and venular insertions in the posterior pole

The number and relative arrangement of arteriolar and venular insertions into the choriocapillaris are key determinants of the shape of functional vascular segments and the blood flow within their domain (Zouache et al., 2016). Maps of arteriolar and venular insertions into the choriocapillaris were extracted from three-dimensional reconstructions of choroids dissected from the posterior pole of three human donor eyes (Sample 1: 64 years old, right eye; Sample 2: 41 years old, right eye; Sample 3: 45 years old, right eye); see Fig. 5*A*. Thirty-three arteriolar insertions were identified in Sample 1, 73 in Sample 2 and 63 in Sample 3. These amounted to densities of 14, 7 and 4 insertions per mm^2 of tissue, respectively. Forty-two venular insertions were identified in Sample 1, 58 in Sample 2 and 122 in Sample 3. These amounted to densities of 19, 6 and 8 insertions per mm^2 of tissue, respectively (see Fig. 5*D*).

The median distance between nearest arteriolar insertions ranged from 130.3 μm (IQR 88 μm) in Sample 1 to 272.5 μm (IQR 125.7 μm) in Sample 3; see Fig. 5*B*. When considering pairwise correlations between the location of arteriolar insertions only, a short-range regularity and departure from a Poisson process was observed in all samples for distances shorter than $r = r_{min}$, with $r_{min} = 66.6\ \mu$m for Sample 1, $r_{min} = 72.4\ \mu$m for Sample 2 and $r_{min} = 93.7\ \mu$m for Sample 3. Since the estimated pairwise correlation function $g(r)$ peaks at $r = r_{min}$, this regularity emerges from short range attractions between arteriolar insertions for $r \leq r_{min}$. The pattern displayed when considering venular insertions only was similar, with short range attractions observed with $r_{min} = 84\ \mu$m for Sample 1, $r_{min} = 80\ \mu$m for Sample 2 and $r_{min} = 82\ \mu$m for Sample 3. Maps of arteriolar insertions only included a region $r_1 \leq r \leq r_2$ where inhibition was observed, with $r_1 = 102\ \mu$m and $r_2 = 133\ \mu$m for Sample 1; $r_1 = 109\ \mu$m and $r_2 = 304\ \mu$m for Sample 2; and $r_1 = 245\ \mu$m and $r_2 = 594\ \mu$m for Sample 3.

The median distance between arteriolar insertions and nearest venular insertion (denoted $r^{a}_{v\ med}$) ranged from 95.9 μm (IQR 60.5 μm) in Sample 1 to 135.3 μm (IQR 194.9 μm) in Sample 3. The estimated pairwise correlation function indicated the presence of short-range attractions between arteriolar and venular insertions

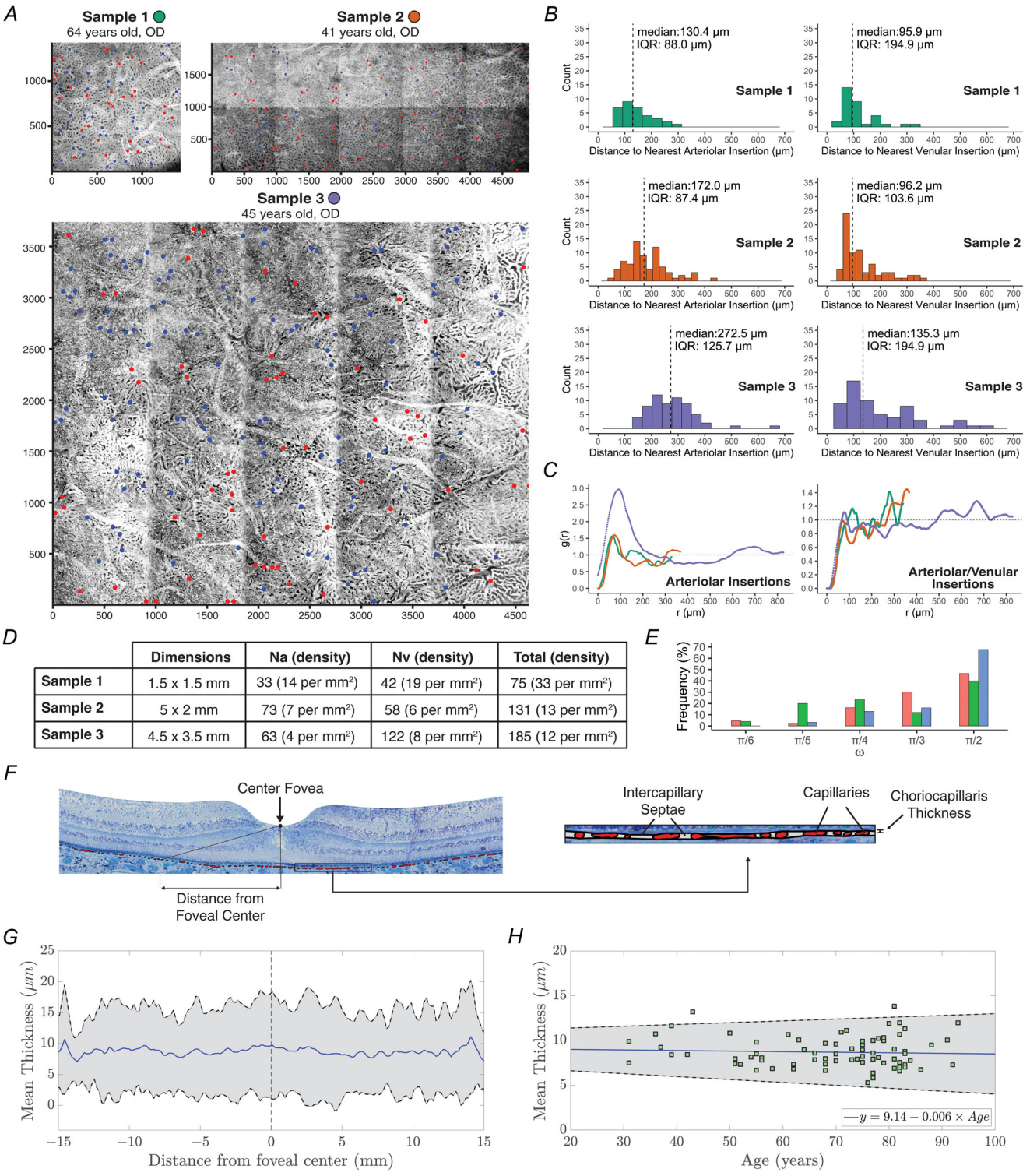

	Dimensions	Na (density)	Nv (density)	Total (density)
Sample 1	1.5 x 1.5 mm	33 (14 per mm²)	42 (19 per mm²)	75 (33 per mm²)
Sample 2	5 x 2 mm	73 (7 per mm²)	58 (6 per mm²)	131 (13 per mm²)
Sample 3	4.5 x 3.5 mm	63 (4 per mm²)	122 (8 per mm²)	185 (12 per mm²)

Figure 5. Relative arrangement of arteriolar and venular insertions into the choriocapillaris and variation of its thickness in the posterior pole
A, maps of arteriolar (●) and venular (●) insertions into the choriocapillaris in portions of choroids dissected from the posterior pole of three healthy human donor eyes. Distances on the horizontal and vertical axes are expressed in μm. *B*, distribution of the distance between arteriolar insertions and the nearest arteriolar or venular insertion, respectively, with median and interquartile range. *C*, estimated pairwise correlation function computed for arteriolar insertions only (left) and arteriolar and venular insertions (right). *D*, characteristics of the samples

dissected and number and density of arteriolar and venular insertions. *E*, distribution of the estimated angle ω between arteriolar insertions and two consecutive venular insertions. *F*, histology section from a human eye with manually delineated capillaries and interpolated inner and outer boundaries of the choriocapillaris. The inner- and outermost borders of the choriocapillaris were delineated by determining the boundary enclosing all capillaries. *G*, variation of the thickness of the choriocapillaris averaged over all sections with distance from the foveal centre and 95% confidence interval. *H*, variation of the choriocapillaris thickness averaged across each section with age. The mean thickness of the choriocapillaris does not vary significantly with age ($P = 0.6$).

and departure from a Poisson process for $r \leq r_{min}$, with $r_{min} = 114\ \mu$m for Sample 1, $r_{min} = 302\ \mu$m for Sample 2 and $r_{min} = 79.2\ \mu$m for Sample 3. For $r \geq r_{min}$, $g(r)$ alternated patterns indicative of inhibition and attraction between these two types of insertion. This variation is consistent with a clustering pattern, with venular insertions clustering around arteriolar ones. The relative arrangement of arteriolar and venular insertions is therefore probabilistically dependent.

The angle between arteriolar insertions and two consecutive venular ones (denoted ω) was estimated from the ratio between these two types of insertion. This ratio was determined by counting the number of venular insertions located within a radius $r = 2r_{med}^{\frac{a}{v}}$ of each arteriolar one. Across all samples, ω ranged from $\frac{\pi}{2}$ to $\frac{\pi}{12}$. The most frequent angle in all samples was $\omega = \frac{\pi}{2}$ (Sample 1: 46.5%, Sample 2: 40%, Sample 3: 67.8%) followed by $\omega = \frac{\pi}{3}$ in Sample 1 (13%) and Sample 3 (16%) and $\omega = \frac{\pi}{4}$ in Sample 2 (24%); see Fig. 5*E*.

Thickness of the choriocapillaris in the posterior pole

The thickness of the choriocapillaris in the posterior pole was assessed by manually segmenting sections 6 mm wide and 1 μm thick of portions of maculas dissected from 81 randomly selected human donor eyes. The age of these donors ranged from 31 to 93 (mean: 68.9 ± 15.1). None of the donors had any recorded eye disorders, and gross photographs and histology sections did not show any sign of retinal or choroidal pathology. The variation of the choriocapillaris thickness with distance from the centre of the fovea was determined by sampling this thickness at approximately 5000 points within each section (see Fig. 5*F*). Over the regions sampled, the thickness of the choriocapillaris did not vary significantly with location (see Fig. 5*G*). Its average among all sampled locations ranged from 6.14 μm to 15.34 μm (mean: $8.82 \pm 1.0\ \mu$m) and remained relatively constant with distance from the foveal centre across all sections. The mean thickness of the choriocapillaris, defined as the average of the thickness over each section, did not vary significantly with age (linear regression, $P = 0.6$); see Fig. 5*H*.

Estimates of choriocapillaris flow and transport parameters

A literature search was performed to determine estimates of choriocapillaris flow parameters (summarized in Table 2). These measurements were all based on angiography of the choriocapillaris performed using either sodium fluorescein or indocyanine green (ICG) as a fluorescent dye. The distance between arteriolar and venular insertions determined from the lobular appearance of the choriocapillaris in human eyes was estimated to lie between 130 and 300 μm (Fujiwara et al., 2007), which is consistent with measurements from human tissue (see Fig. 5*B*). Arteriolar flow rate may be estimated from the mean velocity of blood within the choriocapillaris, here denoted $\bar{u}$. Close to an arteriolar opening, the flow satisfies

$$\bar{u} \simeq \frac{Q_a}{2\pi h^2 \delta}, \tag{27}$$

where $\delta = \frac{R_a}{h}$. Previous analyses of human tissue have found that $6\ \mu\text{m} \leq R_a \leq 32.5\ \mu$m (Fryczkowski, 1994; Torczynski & Tso, 1976); see Table 3. Since we found that $6.14\ \mu\text{m} \leq h \leq 15.34\ \mu$m a conservative estimate is $0.4 \leq \delta \leq 5.3$. Previous reports using experiments performed on rhesus monkeys (Flower et al., 1995), baboons (Kiryu et al., 1994) and Japanese macaques (Takasu et al., 2000) have consistently shown that the mean blood velocity within the choriocapillaris was approximately $\bar{u} = 2.5\ \text{mm.s}^{-1}$. Therefore, the estimated flow rate at an arteriolar insertion lies within the range

$$5.8 \times 10^{-13} \leq Q_a \leq 1.4 \times 10^{-12}\ \text{m}^3.\text{s}^{-1}. \tag{28}$$

The Péclet number at an arteriolar insertion is solute-specific; it satisfies

$$P\,e_a = \frac{Q_a}{DR_a} \simeq \frac{2\pi h \bar{u}_{cc}}{D}. \tag{29}$$

The diffusivity of oxygen in plasma is approximately $D_{ox} = 2 \times 10^{-9}\text{m}^2.\text{s}^{-1}$ (Hershey & Karhan, 1968; Keller & Friedlander, 1966; Spaeth & Friedlander, 1967; Yoshida & Ohshima, 1966), which yields $48 \leq Pe_a^{ox} \leq 120$. For glucose, using $D_{glu} = 7.9 \times 10^{-10}\text{m}^2.\text{s}^{-1}$ (Lindon et al., 1999) we obtain $122 \leq Pe_a^{glu} \leq 305$. Based on the diffusivity of albumen measured in bovine serum $D_{alb} = 2.6 - 6.8 \times 10^{-11}\text{m}^2.\text{s}^{-1}$ (Wakeham et al., 1976), we can infer that Pe_a^{alb} satisfies $1.4 \times 10^3 \leq Pe_a^{alb} \leq 3.5 \times 10^3$.

Table 2. List of choriocapillaris flow parameters collected from published experimental studies through literature review. All measurements are based on angiography (fluorescein or indocyanine green) and were made in the posterior pole

Parameter	Notation	Typical value (method, species)	Reference
Blood mean	$\langle T \rangle_{exp}$	$\leq$ 400 ms (FA, resus monkey)	Perry et al., 1977
Transit time		$\sim$ 125 ms (FA, resus monkey)	Flower, 1980
		118 ± 26 ms (FA, baboon)	Kiryu et al., 1994
		$\sim$ 125 ms (ICGA, resus monkey)	Flower, 1980
Mean blood	$\bar{u}_{cc}$	2.53 ± 0.55 mm.s^{-1} (FA, baboon)	Kiryu et al., 1994
Velocity		2.5 mm.s^{-1} (ICGA, rhesus monkey)	Flower et al., 1995
		2.45 ± 0.48 mm.s^{-1} (ILA, Japanese macaque)	Takasu et al., 2000
		2.5 mm.s^{-1} (rhesus monkey)	Flower et al., 1995
Arteriolar-	L	270 ± 90 μm (FA, rhesus monkey)	Kiryu et al., 1994
Venular distance		$130 - 300$ μm (FA, human)	Fujiwara et al., 2007
		$50 - 250$ μm (ILA, Japanese macaque)	Takasu et al., 2000
Apex angle	ω	$\frac{\pi}{3}, \frac{2\pi}{5}, \frac{\pi}{2}, \frac{2\pi}{3}$ (FA, rhesus monkey)	Hayreh, 1974b
		$\frac{2\pi}{7}, \frac{\pi}{3}, \frac{2\pi}{5}, \frac{\pi}{2}$ (FA, baboon)	Kiryu et al., 1994
Oxygen	D_{ox}	$1.17 - 2 \times 10^{-9}$m^2.s^{-1}	Yoshida & Ohshima, 1966
Diffusivity		$(25 - 37.5^{\circ}$C)	Keller & Friedlander, 1966
			Spaeth & Friedlander, 1967
			Hershey & Karhan, 1968
Glucose diffusivity	D_{gluc}	$7.6 - 7.9 \times 10^{-10}$m^2.s^{-1}	Lindon et al., 1999
Albumen diffusivity	D_{alb}	$7.6 - 7.9 \times 10^{-10}$m^2.s^{-1}	Wakeham et al., 1976
(Bovine serum)		$(25 - 37.5^{\circ}$C)	

FA, fluorescein angiography; ICGA, indocyanine green angiography; ILA, indocyanine-labelled angiography (leukocytes).

Table 3. Quantitative aspects of the geometry of the choriocapillaris in man collected through literature review

Parameter	Notation	Method	Region	Reported value (method, species)	Reference
Thickness	h	Vascular cast	Maculara to periphery	8 $-$ 20 μm	Olver, 1990
		IHC (TS)	Macular Aarea	9.85 μm $-$ 0.033 $\times$ Age	Ramrattan et al., 1994
		IHC (TS)	Macular area	6.9 ± 1.9 μm	Spraul et al., 1996
		IHC (TS)	Periphery	7.5 ± 2.4 μm	Spraul et al., 1996
		IHC (TS)	Macular area	6.9 ± 2.2 μm	Spraul et al., 2002
		IHC (TS)	Posterior pole (TP)	7.7 ± 2.1 μm	Spraul et al., 2002
		IHC (TS)	Posterior pole (NS)	6.2 ± 1.9 μm	Spraul et al., 2002
Radius	R_a	Histology (FP)	Macular area	13.55 μm	Torczynski & Tso, 1976
Arterioles		Histology (FP)	Posterior pole	7.5 $-$ 12.5 μm	Torczynski & Tso, 1976
		Vascular cast	Posterior pole	6 $-$ 21 μm	Fryczkowski, 1994
		Vascular cast	Posterior pole	15 $-$ 32.5 μm	Fryczkowski, 1994
Radius	R_v	Histology (FP)	Macular area	13.55 μm	Torczynski & Tso, 1976
Venules		Histology (FP)	Posterior pole	15 $-$ 18.75 μm	Torczynski & Tso, 1976
		Vascular Cast	Posterior pole	11 $-$ 35 μm	Fryczkowski, 1994
		Vascular Cast	Posterior pole	17.5 $-$ 42.5 μm	Fryczkowski, 1994
Arteriovenous	L	Histology (FP)	Posterior pole	300 $-$ 400 μm	Torczynski & Tso, 1976
Distance		Vascular cast	Macular area	10 $-$ 15 μm	Fryczkowski & Sherman, 1988
		Vascular cast	Posterior pole	200 $-$ 350 μm	Olver, 1990
		Vascular cast	Equatorial region	300 $-$ 400 μm	Olver, 1990
		Vascular cast	Periphery	500 $-$ 1000 μm	Olver, 1990

IHC, immunohistochemistry; TS, tangential section; FP, flat preparation; TP, temporal posterior quadrant; NS, nasal superior quadrant.

Width of diffusion-limited regions

Diffusion-limited regions span areas overlapping boundaries between two adjacent functional vascular segments. Their width, denoted w, satisfies

$$w^2 \sim \frac{2\pi DhL^2 \sin^2(\omega/2)}{Q_a}, \text{ or, } \frac{w^2}{L^2} \sim \frac{2\pi \sin^2(\omega/2)}{\delta Pe_a}. \quad (30)$$

The width of diffusion-limited regions is determined by the balance between anatomical (relative arrangement of arteriolar and venular insertions and the thickness of the choriocapillaris) and functional (arteriolar flow rate, diffusivity) parameters. In order to assess the differential effect of these parameters, it is useful to use the minimum physiologically realistic width as a reference. At constant Pe_a, smallest values of w (denoted w_0) are obtained for closely arranged arterioles and venules ($L \ll 1$) and large values of δ. Since the minimum distance between arteriolar and venular insertions that we measured across samples was $L_0 = 43\ \mu$m, and the largest possible value of δ that we identified is $\delta_0 = 5.3$, we find that the minimum physiologically realistic value of w_0 is

$$w_0(\omega, Pe_a) \simeq L_0\sqrt{\frac{2\pi}{\delta_0}} \times \frac{\sin(\omega/2)}{\sqrt{Pe_a}} = 4.8 \times 10^{-5} \times \frac{\sin(\omega/2)}{\sqrt{Pe_a}}. \quad (31)$$

For $Pe_a = 100$ and within the range of estimated ω (see Fig. 5*E*), $w_0 \sim 1\ \mu$m. Importantly, this estimate was obtained by considering one functional vascular segment only. The minimum physiologically realistic value of w_0 for the entire span of diffusion-limited region along a separation surface is therefore $w_0 \sim 2\ \mu$m. Since it depends on diffusivity, this width is substance specific (see Fig. 6*B*). It is smaller in thinner choriocapillaris and increases as the Péclet number decreases (see Fig. 6*C*). Increasing the distance between arteriolar and venular insertions increases the width of diffusion-limited regions (see Fig. 6*D*), while narrower angles between these insertions reduce it (see Fig. 6*E*).

Diffusion-limited regions represent areas of reduced exchange

The Péclet number in diffusion-limited regions is smaller than that in the channel region. To assess how this affect exchange with the outer retina, we considered the variation of the density flux along the streamline connecting an arteriolar insertion to a stagnation point (see Fig. 6*A*) and compared transfers in diffusion-limited regions to those in the channel region. To account for the effect of anatomical and functional parameters, we normalized the density flux in the channel and diffusion-limited region by their respective value at the entrance of each region. We also considered this variation over distances normalized by the respective width of each region. For w of the order of L, the concentration at the entrance of the diffusion-limited region becomes small so that transfers do not occur across this area. For w smaller than L, the density flux in the diffusion-limited region is systematically lower than its equivalent in the channel region (see Fig. 6*F*). This indicates that exchange between the choriocapillaris and retina are less efficient in diffusion-limited regions, with the lowest transfers observed at the separation surface. This effect becomes more pronounced as the width of diffusion-limited regions increases, as shown in Fig. 6*G*. Diffusion-limited regions therefore consist of regions of comparatively reduced molecular exchange with the outer retina.

Diffusion-limited regions are ubiquitous over the choriocapillaris

The number of diffusion-limited regions (here denoted N_s) is equal to the number of stagnation points N_s present within the flow field. Therefore, this number satisfies (Zouache et al., 2016)

$$N_s = N_a + N_v, \quad (32)$$

where N_a is the number of arteriolar openings and N_v is the number of venular openings. Based on anatomical measurements that we collected, the number of diffusion-limited regions is between 12 and 33 per mm^2 in the posterior pole (see Fig. 5*D*).

Discussion

Planar vascular geometries are generally considered inefficient for mass transfers (LaBarbera, 1990). Yet, photoreceptors, cells that have some of the highest metabolic requirements of any cell in the human body (Linsenmeier & Braun, 1992; Niven & Laughlin, 2008; Wong–Riley, 2010), rely on a planar vascular bed for metabolism and homeostasis. This geometry has several advantages, but also requires some trade-offs. The planar multipolar geometry of the choriocapillaris and its large vascular density maximize the area of the surface available for exchange with the outer retina. High arteriolar flow rate and adjusted arrangement of arteriolar and venular insertions may compensate for the inverse dependence of transfers on distance from arteriolar insertions. This may explain why the average blood velocity in the choriocapillaris needs to be at least twice as fast as that in the retinal vasculature (Takasu et al., 2000). The main trade-off associated with planar multipolar geometries is the necessary presence of diffusion-limited regions, which represent regions of comparatively reduced

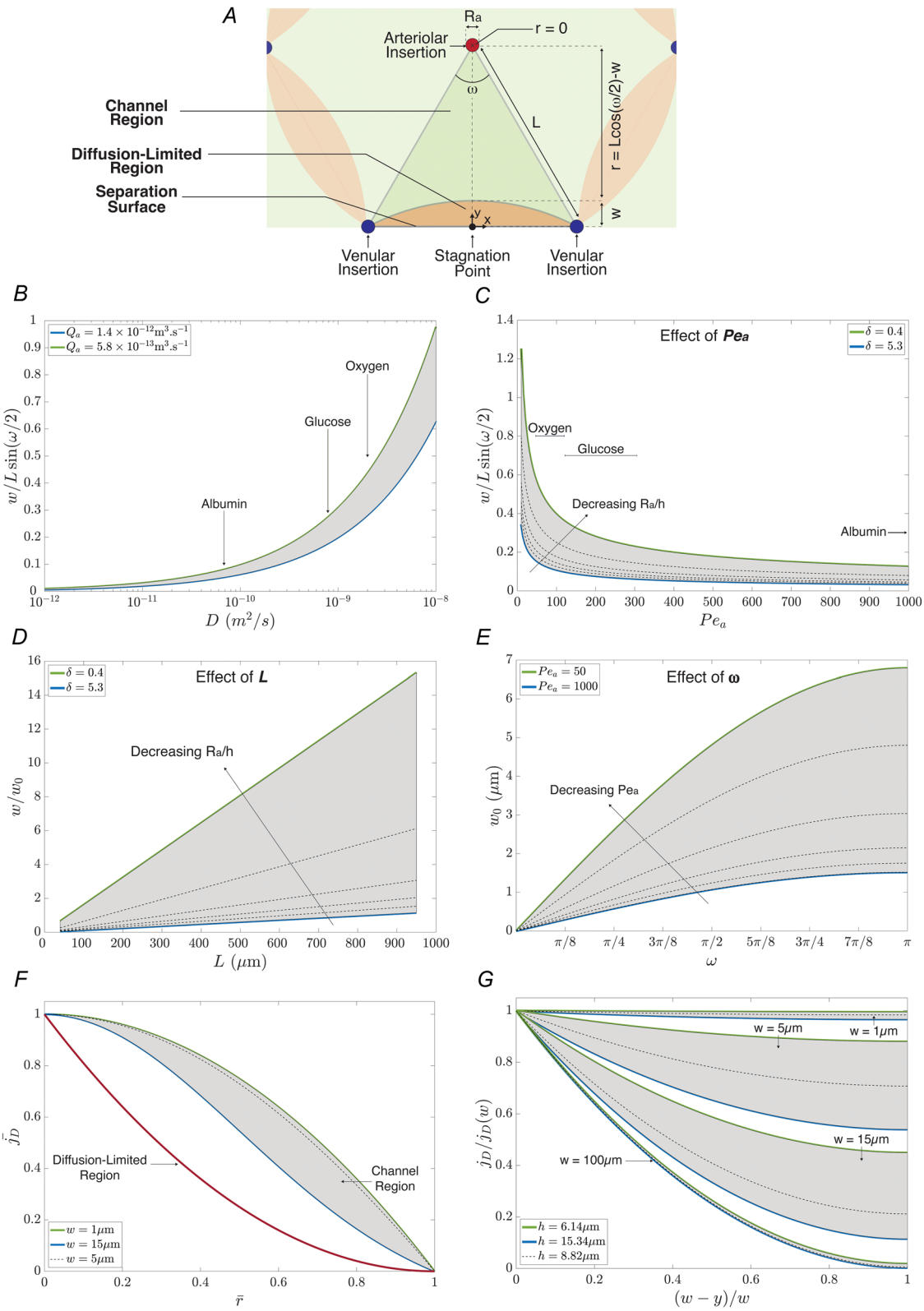

Figure 6. Differential effect of anatomical and functional parameters on the width of diffusion-limited regions and exchange with the outer retina at the scale of a functional vascular segment
A, standard model of an elementary portion of a functional vascular segment. *B–C*, variation of the width of diffusion-limited regions at a stagnation point with (*B*) the diffusivity and (*C*) the Péclet number at an arteriolar

insertion. *D*, variation of the width of diffusion-limited regions at stagnation points normalized by the minimum physiologically observed width w_0 with the distance between arteriolar and venular openings L and the ratio $\delta = \frac{R_a}{h}$. *E*, variation of the width of diffusion-limited regions with the angle ω between an arteriolar insertion and two consecutive venular insertions. *F*, variation of $\bar{j}_D$ with $\bar{r}$, where $\bar{r} = \frac{r}{L\cos(\frac{\omega}{2})-w}$ for the channel region and $\bar{r} = \frac{r-(L\cos(\frac{\omega}{2})-w)}{w}$ for the diffusion-limited region for varying values of w. *G*, variation of $\frac{j_D}{j_D(w)}$ with distance from the boundary between channel and diffusion-limited region for varying values of w and h. Shaded areas indicate the range of values for varying (*B*) Q_a, (*C–D*) $\frac{R_a}{h}$, (*E*) Pe_a, (*F*) w and (*G*) h, respectively.

exchange. However, the contribution of these regions to total exchange with the outer retina may be kept small provided that anatomical and functional parameters are adequately balanced.

This balance may be assessed by characterizing the structure of the choriocapillaris in human eyes. Morphometric analyses of the human choriocapillaris have relied on a variety of techniques including transverse sections (Garron, 1963; Ramrattan et al., 1994; Spraul et al., 1996; Torczynski & Tso, 1976), flat preparations (Hogan & Feeney, 1961; Klien, 1966; Torczynski & Tso, 1976; Yoneya et al., 1983; Zouache et al., 2016), neoprene vascular casts (Ashton, 1952; Weiter & Ernest, 1974; *Wybar, 1954a*, *1954b*) and scanning electron microscopy of corrosion casts (Araki, 1976; Fryczkowski, 1994; Fryczkowski & Sherman, 1988; Fryczkowski et al., 1985, 1989, 1991; Olver, 1990; Yoneya et al., 1983; Zhang, 1994). Only a few of these assessments reported quantitative measurements and no study apart from Ramrattan et al. (1994) implemented sampling strategies or specified the exact locations where measurements were made. Our estimates of choriocapillaris thickness lie within a range similar to those reported previously (Olver, 1990; Ramrattan et al., 1994; Spraul et al., 1996, 2002). However, we did not observe a significant reduction in choriocapillaris thickness with age, as reported by one study (Ramrattan et al., 1994). This difference may be due to the fact that we segmented and quantified regions of the macula almost six times larger in span than this previous investigation. The comparatively larger number of eyes from donors younger than 30 that the previous report included may also partly explain this discrepancy.

No prior study has sought to quantify the distribution of arteriolar and venular insertions into the choriocapillaris. The probabilistically dependent arrangement of both types of insertion underlines a necessary regularity in the structure of the choriocapillaris. This finding is highly significant and demonstrates the balance between structural and functional choriocapillaris parameters normally concealed behind the apparent complexity of this vascular bed. Non-random patterns in the ratio and relative arrangement of the arterioles and venules supplying and draining the capillary beds are also observed in other penetrating vascular beds, including those in the brain (Duvernoy et al., 1981) and in the retina (Stokoe & Turner, 1966; Wise et al., 1975). The clustering of venular insertions around arteriolar ones that we observed in the choriocapillaris is consistent with the general description of functional lobules. Ocular physiologists described these units as being fed by a central arteriole and drained by a series of venules enclosing it (Hayreh, 1974c; Zouache et al., 2016). Short-range attractions between arteriolar insertions may be due to the fact that arterioles often branch into two or more short segments prior to inserting into the plane of the choriocapillaris; although, more detailed analyses are necessary to confirm this. Median distances between arteriolar and venular insertions that we extracted from three samples lie within a range similar to estimates from previous reports (Fryczkowski & Sherman, 1988; Olver, 1990; Torczynski & Tso, 1976). Importantly, they are also consistent with the few measurements made *in vivo* using dye angiography (Fujiwara et al., 2007; Kiryu et al., 1994; Takasu et al., 2000).

To generate predictions on the salient features of mass transfers between choriocapillaris and outer retina, aspects of the geometry, flow and transport characteristics have been idealized. Right angles have been imposed between efferent arterioles and venules and the plane of the choriocapillaris. Bends at the connection between arterioles and the choriocapillaris may reduce pressure losses (Moller, 1966; Nakabayashi et al., 2002) and affect mass transfer locally and downstream of arteriolar insertions. The assumed independence between solute concentration and the viscosity and density of blood is only satisfied when variation in mass within this fluid is small. While eqn (7) is a common boundary condition to apply when investigating salient mass transfer characteristics associated with specific vascular geometries, the limits for which it is a good approximation depend on several factors. These include the physical characteristics of the choriocapillaris/outer retina interface, and solute concentrations in retinal tissue (Zouache et al., 2019). The choriocapillaris has evolved several features that facilitate transfers across endothelial cells, including fenestrations (Zouache, 2022). Refined models are necessary to determine the differential contribution of these structures to mass transfers to the outer retina, including in the vicinity of diffusion-limited regions. The modelling assumption that the thickness of the choriocapillaris remained constant over functional vascular segments was validated by our morphometric

analyses. We were also able to determine physiologically realistic ranges of the angle ω, a key descriptor of the relative arrangement of arteriolar and venular insertions and shape of functional vascular segments (Zouache et al., 2016). A limitation of this study lies in the exclusion of intercapillary septae from our standard model. Previous work indicates that the fundamental properties of the blood flow and advective transport in the choriocapillaris are largely independent from septae. Their presence may increase blood velocity and therefore potentially modify the Péclet number; however, these effects are mainly local (Zouache et al., 2015). Systematic analyses are necessary to investigate the contribution of septae to mass transfers; they will be performed in future studies. In addition, our approach was limited by the fact that only passive solutes were considered. Recent work has, for instance, identified regions of erythrocyte stasis in the human choriocapillaris (Li et al., 2023). This finding is consistent with the presence of regions with stagnation flows within the choriocapillaris predicted by our standard model. Investigating the effect of dominantly advected particles (such as erythrocytes) on transfers to the outer retina requires a separate framework that we hope to develop in the future.

Our study provides a theoretical framework to explore mass exchange between choriocapillaris and outer retina and how they may change in ageing and disease experimentally. The interdependence between anatomical and functional parameters that we uncovered underlines the difficulty in validating the predictions of mathematical models. The salient features of mass transfers between choriocapillaris and outer retina may be inferred from oxygen concentration profiles extracted invasively from animal eyes (Linsenmeier & Zhang, 2017). Measures of veno–arterial difference in the concentration of glucose and oxygen obtained from the choroid of cats and pigs have been used to estimate bulk transfers between choriocapillaris and outer retina (Wang, Kondo et al., 1997; Wang, Törnquist et al., 1997; Zouache, 2022; Zouache et al., 2016). These methods are, however, not adapted to detect spatial variabilities in transfers at the scale of a group of functional lobules. In addition, they do not allow for the simultaneous extraction of anatomical and functional parameters that are key to quantifying mass transfers and their variation. Multipolar microfluidic systems, which mimic the vascular geometry of the choriocapillaris, offer promising ways of validating the predictions of mathematical models. Diffusion-limited regions are experimentally observed in multipolar devices (Goyette et al., 2019; Qasaimeh et al., 2011), and have been harnessed to generate tunable linear concentration gradients (Qasaimeh et al., 2011). In addition to improving our understanding of mass transfers between choriocapillaris and outer retina, the mathematical framework that we laid out in this study may therefore be used to inform the design of multipolar microfluidic systems, with applications ranging from the study of cell chemotaxis, single-cell analyses (Boulais & Gervais, 2023), and groundwater, hydrocarbon and geothermal heat recovery (Koplik et al., 1994; Kurowski et al., 1994; Zhang & Koplik, 1997).

The contribution of diffusion-limited regions to exchange with the outer retina is likely to increase in ageing and in disease. Choroidal blood flow and volume decrease by 7.5 and 8.8% per decade on average, respectively (Zouache, 2022). The associated reduction in arteriolar flow rate would increase the width of the diffusion-limited region and therefore create broad areas with significantly reduced exchange with the outer retina. This phenomenon may be linked to the spatial selectivity of pathologies associated with retinal diseases including AMD (Friedman et al., 1963; Müller, 1856; Tso, 1985; *Wybar, 1954a*). Future work built upon the findings of the present study will be performed to confirm these associations.

References

Abramoff, M. D., Magalhaes, P. J., & Ram, P. J. (2004). Image processing with imageJ. *Biophotonics International*, **11**(7), 36–42.

Abramowitz, M., & Stegun, I. A. (1972). *Handbook of Mathematical Functions: With Formulas, Graphs, and Mathematical Tables, 9th printing*. Dover, New-York.

Araki, M. (1976). Observations on the corrosion casts of the choriocapillaries. *Acta Societatis Ophthalmologicae Japonicae*, **80**, 315–325.

Archer, D., Krill, A. E., & Newell, F. W. (1970). Fluorescein studies of normal choroidal circulation. *American Journal of Ophthalmology*, **69**(4), 543–554.

Ashton, N. (1952). Observations on the choroidal circulation. *British Journal of Ophthalmology*, **36**(9), 465–481.

Baddeley, A., Rubak, E., & Turner, R. (2015). *Spatial point patterns: Methodology and applications with R*. CRC Press, Taylor & Francis Group, Boca Raton.

Baddeley, A., & Turner, R. (2005). Spatstat : An*r* package for analyzing spatial point patterns. *Journal of Statistical Software*, **12**(6), 1–42.

Bill, A., Sperber, G., & Ujiie, K. (1983). Physiology of the choroidal vascular bed. *International Ophthalmology*, **6**(2), 101–107.

Boulais, E., & Gervais, T. (2023). The 2D microfluidics cookbook - modeling convection and diffusion in plane flow devices. *Lab on A Chip*, **23**(8), 1967–1980.

Ciulla, T. A., Harris, A., Chung, H. S., Danis, R. P., Kagemann, L., McNulty, L., Pratt, L. M., & Martin, B. J. (1999). Color Doppler imaging discloses reduced ocular blood flow velocities in nonexudative age-related macular degeneration. *American Journal of Ophthalmology*, **128**(1), 75–80.

Duvernoy, H. M., Delon, S., & Vannson, J. L. (1981). Cortical blood vessels of the human brain. *Brain Research Bulletin*, **7**(5), 519–579.

Feeney, A. B. L., & Hogan, M. J. (1961). Electron microscopy of the human choroid. II. The choroidal nerves. *American Journal of Ophthalmology*, **51**(5), 1072/200–1083/211.

Fletcher, J. E. (1978). Mathematical modeling of the microcirculation. *Mathematical Biosciences*, **38**(3–4), 159–202.

Flower, R. W., Fryczkowski, A. W., & McLeod, D. S. (1995). Variability in choriocapillaris blood flow distribution. *Investigative Ophthalmology & Visual Science*, **36**(7), 1247–1258.

Flower, R. W. (1993). Extraction of choriocapillaris hemodynamic data from ICG fluorescence angiograms. *Investigative Ophthalmology & Visual Science*, **34**(9), 2720–2729.

Friedman, E., R Smith, T., & Kuwabara, T. (1963). Senile choroidal patterns and drusen. *Archives of Ophthalmology*, **69**, 114–124.

Fryczkowski, A. W., Grimson, B. S., & Peiffer, R. L. (1985). Vascular casting and scanning electron microscopy of human ocular vascular abnormalities. *Archives of Ophthalmology*, **103**(1), 118–120.

Fryczkowski, A. W., Hodes, B. L., & Walker, J. (1989). Diabetic choroidal and iris vasculature scanning electron microscopy findings. *International Ophthalmology*, **13**(4), 269–279.

Fryczkowski, A. W., Sherman, M. D., & Walker, J. (1991). Observations on the lobular organization of the human choriocapillaris. *International Ophthalmology*, **15**(2), 109–120.

Fryczkowski, A. W., & Sherman, M. D. (1988). Scanning electron microscopy of human ocular vascular casts: The submacular choriocapillaris. *Acta Anatomica*, **132**(4), 265–269.

Fryczkowski, A. W. (1994). Anatomical and functional choroidal lobuli. *International Ophthalmology*, **18**(3), 131–141.

Fujiwara, T., Iida, T., & Kanda, N. (2007). Lobular structure of the choriocapillaris in a patient with ophthalmic artery occlusion. *Japanese Journal of Ophthalmology*, **51**, 477–481.

Garron, L. K. (1963). The ultrastructure of the retinal pigment epithelium with observations on the choriocapillaris and Bruch's membrane. *Transactions of the American Ophthalmological Society*, **61**, 545–588.

Geuzaine, C., & Remacle, J.-F. (2009). Gmsh: A 3-D finite element mesh generator with built-in pre- and post-processing facilities. *International Journal for Numerical Methods in Engineering*, **79**(11), 1309–1331.

Goyette, P.-A., Boulais, É., Normandeau, F., Laberge, G., Juncker, D., & Gervais, T. (2019). Microfluidic multipoles theory and applications. *Nature Communications*, **10**(1), 1781.

Hayreh, S. S. (1974a). Vascular pattern of the choriocapillaris. *Experimental Eye Research*, **19**(1), 101–104.

Hayreh, S. S. (1974b). Recent advances in fluorescein fundus angiography. *British Journal of Ophthalmology*, **58**(4), 391–412.

Hayreh, S. S. (1974c). The choriocapillaris. *Albrecht Von Graefes Archiv Fur Klinische Und Experimentelle Ophthalmologie*, **192**(3), 165–179.

Hayreh, S. S. (1975). Segmental nature of the choroidal vasculature. *British Journal of Ophthalmology*, **59**(11), 631–648.

Health Organisation, W. (2014). *Global Health Estimates: Deaths by Cause, Age, Sex and Country, 2000–2012*. Geneva, World Health Organisation.

Hershey, D., & Karhan, T. (1968). Diffusion coefficients for oxygen transport in whole blood. *AIChE Journal*, **14**(6), 969–972.

Hirata, Y., Nishiwaki, H., Miura, S., Ieki, Y., Honda, Y., Yumikake, K., Sugino, Y., & Okazaki, Y. (2004). Analysis of choriocapillaris flow patterns by continuous laser-targeted angiography in monkeys. *Investigative Ophthalmology & Visual Science*, **45**(6), 1954–1962.

Hogan, M. J., & Feeney, A. B. L. (1961). Electron microscopy of the human choroid. III. The blood vessels. *American Journal of Ophthalmology*, **51**(5), 1084/212–1097/225.

Hyvarinen, L., Maumenee, A. E., George, T., & Weinstein, G. W. (1969). Fluorescein angiography of the choriocapillaris. *American Journal of Ophthalmology*, **67**(5), 653–666.

Keller, K. H., & Friedlander, S. K. (1966). The steady-state transport of oxygen through hemoglobin solutions. *Journal of General Physiology*, **49**, 663–679.

Kiryu, J., Shahidi, M., Mori, M. T., Ogura, Y., Asrani, S., & Zeimer, R. (1994). Noninvasive visualization of the choriocapillaris and its dynamic filling. *Investigative Ophthalmology & Visual Science*, **35**(10), 3724–3731.

Klien, B. A. (1966). Regional and aging characteristics of the normal choriocapillaris in flat preparations*. *American Journal of Ophthalmology*, **61**(5), 1191–1197.

Koplik, J., Redner, S., & Hinch J., E (1994). Tracer dispersion in planar multipole flows. *Physical Review E*, **50**(6), 4650–4671.

Krogh, A. (1919a). The number and distribution of capillaries in muscles with calculations of the oxygen pressure head necessary for supplying the tissue. *Journal of Physiology (London)*, **52**(6), 409–415.

Krogh, A. (1919b). The supply of oxygen to the tissues and the regulation of the capillary circulation. *Journal of Physiology (London)*, **52**(6), 457–474.

Kurowski, P., Ippolito, I., P Hulin, J., Koplik, J., & J Hinch, E. (1994). Anomalous dispersion in a dipole flow geometry. *Physics of Fluids*, **6**, 108–117.

Replogle, R. L., Meiselman, H. J., & Merrill, E. W. (1967). Clinical implications of blood rheology studies. *Circulation*, **36**, 148–160.

LaBarbera, M. (1990). Principles of design of fluid transport systems in zoology. *Science*, **249**(4972), 992–1000.

Lighthill, M. J. (1972). Physiological fluid dynamics: a survey? *Journal of Fluid Mechanics*, **52**(3), 475–497.

Lindon, J. C., Liu, M., & Nicholson, J. K. (1999). Diffusion coefficient measurement by high resolution NMR spectroscopy: Biochemical and pharmaceutical applications. *Reviews in Analytical Chemistry*, **18**(1-2), 23-66.

Linsenmeier, R. A., & Braun, R. D. (1992). Oxygen distribution and consumption in the cat retina during normoxia and hypoxemia. *Journal of General Physiology*, **99**(2), 177–197.

Linsenmeier, R. A., & Zhang, H. F. (2017). Retinal oxygen: From animals to humans. *Progress in Retinal and Eye Research*, **58**, 115–151.

Li, J., Wang, D., Pottenburgh, J., Bower, A. J., Asanad, S., Lai, E. W., Simon, C., Im, L., Huryn, L. A., Tao, Y., Tam, J., & Saeedi, O. J. (2023). Visualization of erythrocyte stasis in the living human eye in health and disease. *Iscience*, **26**(1), 105755.

Mendrinos, E., & Pournaras, C. J. (2009). Topographic variation of the choroidal watershed zone and its relationship to neovascularization in patients with age-related macular degeneration. *Acta Ophthalmology*, **87**(3), 290–296.

Moller, P. S. (1966). A radial diffuser using incompressible flow between narrowly spaced disks. *Journal of Basic Engineering*, **88**(1), 155–162.

Müller, H. (1856). Anatomische beiträge zur ophthalmologie. *Graefes Archiv für Ophthalmologie*, **2**(2), 1–69.

Mullins, R. F., Johnson, M. N., Faidley, E. A., Skeie, J. M., & Huang, J. (2011). Choriocapillaris vascular dropout related to density of drusen in human eyes with early age-related macular degeneration. *Investigative Ophthalmology & Visual Science*, **52**(3), 1606–1612.

Murray, C. D. (1926). The physiological principle of minimum work. I. The vascular system and the cost of blood volume. *Proceedings of the National Academy of Sciences of the United States of America*, **12**, 207–214.

Nakabayashi, K., Ichikawa, T., & Morinishi, Y. (2002). Size of annular separation bubble around the inlet corner and viscous flow structure between two parallel disks. *Experiments in Fluids*, **32**(4), 425–433.

Niven, J. E., & Laughlin, S. B. (2008). Energy limitation as a selective pressure on the evolution of sensory systems. *Journal of Experimental Biology*, **211**(Pt 11), 1792–1804.

Olver, J. M. (1990). Functional anatomy of the choroidal circulation: Methyl methacrylate casting of human choroid. *Eye (London, England)*, **4**(Pt 2), 262–272.

Parver, L. M. (1991). Temperature modulating action of choroidal blood flow. *Eye (London, England)*, **5**(Pt 2), 181–185.

Pauleikhoff, D., Spital, G., Radermacher, M., Brumm, G. A., Lommatzsch, A., & Bird, A. C. (1999). A fluorescein and indocyanine green angiographic study of choriocapillaris in age-related macular disease. *Archives of Ophthalmology*, **117**(10), 1353–1358.

Perry, H. D., Hatfield, R. V., & Tso, M. O. (1977). Fluorescein pattern of the choriocapillaris in the neonatal rhesus monkey. *American Journal of Ophthalmology*, **84**(2), 197–204.

Pries, A. R., Secomb, T. W., Gessner, T., Sperandio, M. B., Gross, J. F., & Gaehtgens, P. (1994). Resistance to blood flow in microvessels in vivo. *Circulation Research*, **75**(5), 904–915.

Qasaimeh, M. A., Gervais, T., & Juncker, D. (2011). Microfluidic quadrupole and floating concentration gradient. *Nature Communications*, **2**, 464.

Ramrattan, R. S., van der Schaft, T. L., Mooy, C. M., de Bruijn, W. C., Mulder, P. G., & de Jong, P. T. (1994). Morphometric analysis of Bruch's membrane, the choriocapillaris, and the choroid in aging. *Investigative Ophthalmology & Visual Science*, **35**(6), 2857–2864.

Ranvier, L. (1874). Note sur les Vaisseaux Sanguins et la circulation dans les muscles rouges. *Arch Physiology Norm Path*, **1**, 445–450.

Salzman, M. (1912). *The Anatomy and Histology of the Human Eyeball in the Normal State, Its Development and Senescence*. Trans by E. V. L. Brown, The University of Chicago Press.

Seddon, J. M., McLeod, D. S., Bhutto, I. A., Villalonga, M. B., Silver, R. E., Wenick, A. S., Edwards, M. M., & Lutty, G. A. (2016). Histopathological insights into choroidal vascular loss in clinically documented cases of age-related macular degeneration. *JAMA Ophthalmology*, **134**(11), 1272–1280.

Spaeth, E. E., & Friedlander, S. K. (1967). The diffusion of oxygen, carbon dioxide, and inert gas in flowing blood. *Biophysical Journal*, **7**(6), 827–851.

Spalteholtz, W. (1888). Die Vertheilung der Blutgefasse in Muskel. *Abh Sächs Ges Wiss Math Phys*,.

Spraul, C. W., Lang, G. E., Grossniklaus, H. E., & Lang, G. K. (1999). Histologic and morphometric analysis of the choroid, Bruch's membrane, and retinal pigment epithelium in postmortem eyes with age-related macular degeneration and histologic examination of surgically excised choroidal neovascular membranes. *Survey of Ophthalmology*, **44**(Suppl 1), S10-32.

Spraul, C. W., Lang, G. E., & Grossniklaus, H. E. (1996). Morphometric analysis of the choroid, Bruch's membrane, and retinal pigment epithelium in eyes with age-related macular degeneration. *Investigative Ophthalmology & Visual Science*, **37**(13), 2724–2735.

Spraul, C. W., Lang, G. E., Lang, G. K., & Grossniklaus, H. E. (2002). Morphometric changes of the choriocapillaris and the choroidal vasculature in eyes with advanced glaucomatous changes. *Vision Research*, **42**(7), 923–932.

Stokoe, N. L., & Turner, R. W. (1966). Normal retinal vascular pattern. Arteriovenous ratio as a measure of arterial calibre. *British Journal of Ophthalmology*, **50**(1), 21–40.

Dollery C. T., Henkind, P., Kohner, E. M., & Paterson J. W. (1968). Effect of raised intraocular pressure on the retinal and choroidal circulation. *Investigative Ophthalmology & Visual Science*, **7**(2), 191–198.

Takasu, I., Shiraga, F., Okanouchi, T., Tsuchida, Y., & Ohtsuki, H. (2000). Evaluation of leukocyte dynamics in choroidal circulation with indocyanine green–stained leukocytes. *Investigative Ophthalmology & Visual Science*, **41**(10), 2844–2848.

Team, R. C. (2021). R: A Language and Environment for Statistical Computing.

Torczynski, E., & Tso, M. O. (1976). The architecture of the choriocapillaris at the posterior pole. *American Journal of Ophthalmology*, **81**(4), 428–440.

Tso, M. O. (1985). Pathogenetic factors of aging macular degeneration. *Ophthalmology*, **92**(5), 628–635.
Flower, R. W. (1980). Choroidal fluorescent dye filling patterns: A comparison of high speed indocyanine green and fluorescein angiograms. *International Ophthalmology*, **2**, 143.
Wakeham, W. A., Salpadoru, N. H., & Caro, C. G. (1976). Diffusion coefficients for protein molecules in blood serum. *Atherosclerosis*, **25**(2–3), 225–235.
Wang, L., Kondo, M., & Bill, A. (1997). Glucose metabolism in cat outer retina. Effects of light and hyperoxia. *Investigative Ophthalmology & Visual Science*, **38**(1), 48–55.
Wang, L., Törnquist, P., & Bill, A. (1997). Glucose metabolism in pig outer retina in light and darkness. *Acta Physiologica Scandinavica*, **160**(1), 75–81.
Weiter, J. J., & Ernest, J. T. (1974). Anatomy of the choroidal vasculature. *American Journal of Ophthalmology*, **78**(4), 583–590.
Wei, X., Balne, P. K., Meissner, K. E., Barathi, V. A., Schmetterer, L., & Agrawal, R. (2018). Assessment of flow dynamics in retinal and choroidal microcirculation. *Survey of Ophthalmology*, **63**(5), 646–664.
West, G. B., Brown, J. H., & Enquist, B. J. (1997). A general model for the origin of allometric scaling laws in biology. *Science*, **276**(5309), 122–126.
Wise, G. N., Dollery, C. T., & Henkind, P. (1975). *The Retinal Circulation*. Harper and Row, New York.
Wong-Riley, M. T. T. (2010). Energy metabolism of the visual system. *Eye Brain*, **2**, 99–116.
Wong, W. L., Su, X., Li, X., Cheung, C. M. G., Klein, R., Cheng, C.-Y., & Wong, T. Y. (2014). Global prevalence of age-related macular degeneration and disease burden projection for 2020 and 2040: A systematic review and meta-analysis. *The Lancet Global Health*, **2**(2), e106–e116.
Wybar, K. C. (1954a). Vascular anatomy of the choroid in relation to selective localization of ocular disease. *British Journal of Ophthalmology*, **38**(9), 513–527.
Wybar, K. C. (1954b). A study of the choroidal circulation of the eye in man. *Journal of Anatomy*, **88**(1), 94–98.
Yoneya, S., Tso, M. O., & Shimizu, K. (1983). Patterns of the choriocapillaris. A method to study the choroidal vasculature of the enucleated human eye. *International Ophthalmology*, **6**(2), 95–99.
Yoshida, F., & Ohshima, N. (1966). Diffusivity of oxygen in blood serum. *Journal of Applied Physiology*, **21**(3), 915–919.
Zhang, H. R. (1994). Scanning electron-microscopic study of corrosion casts on retinal and choroidal angioarchitecture in man and animals. *Progress in Retinal and Eye Research*, **13**(1), 243–270.
Zhang, M., & Koplik, J. (1997). Tracer dispersion in three-dimensional multipole flows. *Physical Review E*, **56**(4), 4244–4258.
Zouache, M. A., Eames, I., Klettner, C. A., & Luthert, P. J. (2016). Form, shape and function: Segmented blood flow in the choriocapillaris. *Scientific Reports*, **6**, 35754.
Zouache, M. A., Eames, I., Klettner, C. A., & Luthert, P. J. (2019). Flow and passive transport in planar multipolar flows. *Journal of Fluid Mechanics*, **858**, 184–227.
Zouache, M. A., Eames, I., & Luthert, P. J. (2015). Blood flow in the choriocapillaris. *Journal of Fluid Mechanics*, **774**, 37–66.
Zouache, M. A. (2022). Variability in retinal neuron populations and associated variations in mass transport systems of the retina in health and aging. *Frontiers in aging neuroscience*, **14**, 778404.

Additional information

Data availability statement

Raw data are available upon request to M.A.Z. (moussa.zouache@hsc.utah.edu). All other data are included in the manuscript.

Competing interests

G.S.H. is a shareholder, consultant and co-founder of Perceive Biotherapeutics Inc. None of the authors have any relevant proprietary interests.

Author contributions

C.F.: Acquisition and analysis of data; data curation; writing–reviewing. C.K.: Acquisition and analysis of data; data curation; writing–reviewing. M.T.: Acquisition of data; data curation. G.S.H.: Acquisition of data; data curation. I.E.: Analysis of data; interpretation of data, writing–reviewing. P.J.L.: Interpretation of data, writing–reviewing. M.A.Z.: Conceptualisation; study design; methodology; acquisition of data; formal analyses and interpretation of data; project administration; project supervision; validation; visualization; writing. original draft; writing. reviewing and editing. All authors have read and approved the final version of this manuscript and agreed to be accountable for all aspects of the work.

Funding

This work was supported in part by the Leverhulme Trust Research Project Grant RPG-2015-276 (P.J.L. & I.E.), the National Eye Institute of the National Institutes of Health under award numbers R24EY017404 (G.S.H.). Additional support from an unrestricted grant from Research to Prevent Blindness, New York, NY, to the Department of Ophthalmology & Visual Sciences, University of Utah (M.A.Z. & G.S.H.). This work was also partly supported by a generous donation from the Fenton Family Foundation (M.A.Z.).

Acknowledgements

The authors acknowledge the use of the University College London's Myriad High Performance Computing Facility

(Myriad@UCL), and associated support services, in the completion of this work. The support and resources from the Center for High Performance Computing at the University of Utah are gratefully acknowledged. The Authors also acknowledge the use of resources from the Sharon Eccles Steele Center for Translational Medicine, John A. Moran Eye Center, University of Utah, USA, including the eye repository managed by J. Mohler, C. M. Pappas and S. Matthews.

Keywords

blood flow, choriocapillaris, mass transport, retina, retinal homeostasis

Supporting information

Additional supporting information can be found online in the Supporting Information section at the end of the HTML view of the article. Supporting information files available:

Peer Review History